Interaction of 1.3-μm laser radiation with thin foil targets

K. Eidmann, F. Amiranoff,* R. Fedosejevs,† A. G. M. Maaswinkel,‡ R. Petsch,§ R. Sigel, G. Spindler,** Yung-lu Teng,†† G. Tsakiris, and S. Witkowski
Max-Planck-Institut für Quantenoptik, D-8046 Garching, Federal Republic of Germany
(Received 6 March 1984)

Comprehensive studies of the hydrodynamics and energy transport in laser-produced plasmas are presented. Thin low-Z foil targets (10^{-5}–10^{-3} g/cm^2) were irradiated with 300-ps pulses from the Asterix-III iodine laser ($\lambda=1.3$ μm). Different diagnostics such as high-speed photography, plasma calorimetry, Ulbricht sphere for laser-light absorption measurements, and x-ray and ion techniques were used. Results on the velocity and energy of the accelerated foil, pressure, ablation rate, and lateral energy spread were obtained for a wide intensity range 10^{11}–10^{16} W/cm^2. Pressures exceeding 10 Mbar and foil velocities of up to 10^8 cm/s were observed. The experimental data are compared with one-dimensional hydrodynamic calculations using different values of electron heat-flux limitation. An indication of intensity-dependent flux inhibition was found: $f\geq 0.1$ at intensities below 10^{13} W/cm^2, but $f=0.015$–0.03 at intensities above 10^{14} W/cm^2.

I. INTRODUCTION

Intense laser radiation incident on a solid target creates a hot and dense plasma on the irradiated surface.[1] The high pressure exerted by the plasma may accelerate a thin foil target to very high velocities. Figure 1 illustrates this process in a simplified way. A planar foil of total mass m_F is irradiated by a laser pulse. Some part of the foil, the mass m_a is heated and ablated by the laser and, after irradiation, moves with an average velocity v_a towards the laser. As a consequence of the momentum balance $m_a v_a = MV$, the residual mass M then moves with the velocity V to the other side. The efficiency of kinetic energy transfer on the accelerated residual mass is approximated by this model as

$$\eta=\frac{MV^2/2}{MV^2/2+m_a v_a^2/2}$$

or

$$\eta=\frac{m_a}{m_F}\ . \tag{1}$$

Thus, if the foil is not too thick compared with the ablated depth, the residual mass is accelerated to extremely high velocities of the order of the ablation velocity v_a. For example, with lasers of energies around 100 J and pulse durations around 1 ns, one can accelerate masses in the μg region to velocities exceeding 10^7 cm/s. Such velocities are, to our knowledge, the highest obtained with macroparticles in a laboratory.

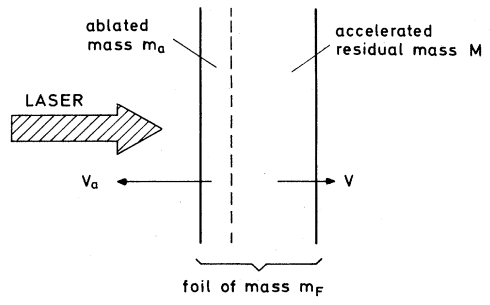

FIG. 1. Simplified scheme of foil acceleration by laser.

The biggest motivation at present for the study of this acceleration process is afforded by the concept of inertial confinement, which requires efficient inward acceleration of a thin pellet shell.[2] Besides this important application, high-velocity macroparticles may in themselves be of interest, e.g., for simulating hypervelocity micrometeroids[3] or for fuelling fusion reactors.[4] The generated pressures exceeding 10 Mbar (Refs. 5–7) are also of interest for studies of the equation of state.[8]

It is evident from Eq. (1) that the detailed physics of laser-induced mass ablation is very important for target acceleration. The essential processes involved are laser-light absorption and the energy transport from the absorption region to the dense part of the target.[9]

Owing to the strong interest in laser fusion these processes are under investigation in many laboratories throughout the world.[10–19] The most detailed study was conducted by the Naval Research Laboratory.[10–12] The aim of this study was to demonstrate ablative acceleration of plane thin foil targets with longer pulses (3 ns) and in a lower intensity range ($\leq 10^{14}$ W/cm^2). Under these conditions the absorption and transport are expected to be dominated by collisions without complications due to collisionless anomalies, which are typically observed at higher intensities.[9,16–20]

This paper presents an extensive series of acceleration experiments with shorter (300 ps) laser pulses that were conducted during the last few years in our laboratory.[21–25] The Asterix III high-power iodine laser ($\lambda=1.3$ μm) was used for irradiation. The aim is to clarify the laser-plasma interaction, the energy transport, and the hydrodynamics in a wide range of incident intensities from 10^{11} to 10^{16} W/cm^2. Typical of this work is the study of

the transition from the collisional "normal" behavior at low intensities to the more complex situation at high intensities. The short pulse used in this experiment together with a larger spot (typically 400 μm) has the advantage of fewer lateral effects caused by lateral heat conduction or by divergence of the plasma flow than in experiments with longer laser pulses, in which such lateral effects become important.[16] Our experiments show that even with the smallest spots used (60 μm) lateral transport effects are not dominant. This facilitates interpretation of the results, because no complicated two-dimensional models are necessary.

A variety of different and independent diagnostic techniques were used. The principal techniques for studying the foil acceleration were high-speed photography, which allows two-dimensional time-resolved observation of the foil motion during and after irradiation, and plasma calorimetry, by which the energy transfered to the target was measured. From these measurements we derive the mass ablation rates and ablation pressures. To cross-check these results, we also determined the mass ablation rate by x-ray spectroscopy with layered targets and the shock pressure due to shock propagation in transparent targets. In addition, we measured the absorption and also the transmission of laser light through very thin foils which become underdense during irradiation.

At high intensities, fast-ion and hot-electron phenomena become important. We measured the emitted x-ray continuum and ion velocity spectra in the expanding plasma. The considerable fraction of energy coupled into hot electrons may be deposited in the dense target material and thus contribute to preheating it. Lateral transport along the target surface away from the irradiated spot may also occur. To obtain information on such transport phenomena, we used ion detectors positioned at the front and the rear side of the foil and studied the bilateral expansion of laser-heated foils. We also used x-ray spectroscopy for spatially resolved observation of the $K\alpha$ emission excited by hot electrons in different regions of the target.

For interpretation of the experimental results the foil acceleration process was simulated by a hydrodynamic code, which includes flux inhibition for the electron transport.[9,20] The comparison of the calculated and measured results yields information on the electron energy transport.

The paper is organized as follows. Section II gives details of the irradiation conditions and the experimental setup. Experimental results for the absorption, electron temperatures, ion velocities, energy transfer to the foil, the foil velocity, the mass ablation rate, the ablation pressure, and lateral transport effects are presented in Sec. III. In Sec. IV there follows an interpretation on the basis of hydrodynamic calculations. The conclusions are given in Sec. V.

II. EXPERIMENTAL SETUP

The scheme of the experimental setup is shown in Fig. 2. The Asterix III iodine laser ($\lambda = 1.3$ μm) used for target irradiation consists of an acousto-optically mode-locked oscillator followed by a single-pulse selection system and four amplifiers to give a maximum output energy of 300 J in about 300 ps. The beam is linearly polarized. Details of the laser system are described in Ref. 26. A small fraction of the output beam is reflected by a beam splitter for diagnostics of the pulse energy, temporal pulse shape, and spatial beam quality of the incident beam.

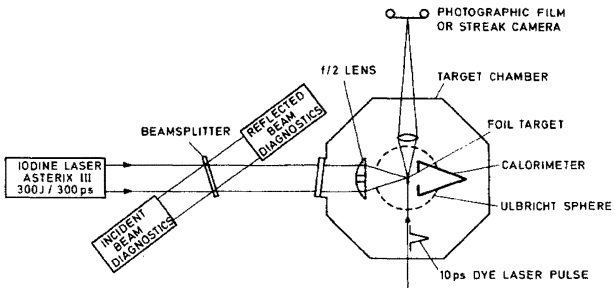

FIG. 2. Scheme of the experimental setup.

The temporal pulse shape was measured with a streak camera with a time resolution of 20 ps and a dynamic range ≤ 10. In addition, a vacuum photodiode (rise time $\cong 100$ ps) coupled to a 1.5-GHz oscilloscope was used to obtain the pulse shape in a larger dynamic range. A typical laser pulse is shown in Fig. 3. The pulse shape may slightly change in different shots, depending on the state of the laser. The average pulse width in these experiments was 280 ± 60 ps full width at half maximum. Irradiation of the target at earlier times before the main pulse hits the target was monitored with a prepulse detector (photomultiplier with S1 cathode), which indicated prepulses with a power exceeding 100 W on target at a time resolution of 3 ns. The energy of mode-lock pulses passing the closed pulse cutter did not exceed 1 μJ at the laser output; contributions due to amplified spontaneous emission and self-oscillations were less than 100 W. High-speed photographs of the target confirmed that these prepulse values are sufficiently low to avoid target damage before the arrival of the main pulse. The beam was focused with an aspherical $f/2$ lens. By changing either the laser energy or the distance between the target

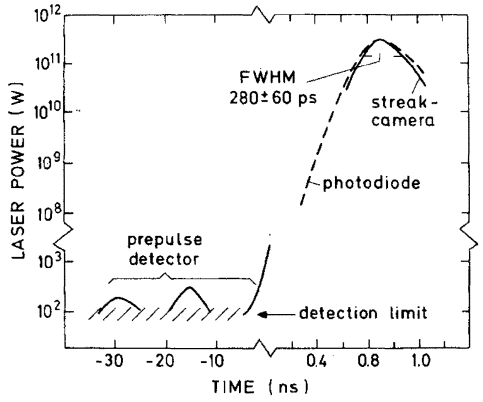

FIG. 3. Laser pulse as measured by streak camera, vacuum photodiode and prepulse detector; incident energy was 100 J.

and the lens the intensity was varied between 10^{11} and 10^{16} W/cm^2. In the case of target positions out of focus we always placed the target between the focus and the lens. Spot sizes ranged from 60 (focus) to 1600 μm. The position of the focus was determined by using a Hartmann plate method with an accuracy of ± 40 μm; for details see Ref. 27.

Typical intensity distributions for two different target positions are shown in Fig. 4. Curve *b* for the target 1 mm out of focus was recorded on photographic infrared film in an equivalent plane when the beam was focused by a focusing mirror of large focal length. The intensity increases from the center to the periphery by a factor of 2 owing to increased gain in the outer zones of the laser amplifiers. The observed diffraction rings are caused by apertures in the laser setup. Because of the hole in the actual *f*/2 focusing lens the intensity decreases near the axis if the target is out of focus, as indicated by the dashed line *b'*. The intensity distribution in focus (curve *a*) was derived from curve *c*, which shows the direct measurement of the energy fraction transmitted through pinholes of different radii positioned in the focal plane of the aspherical *f*/2 lens. Half of the laser energy is contained in a 60-μm-diam aperture.

Thin plastic films were used as targets [Zapon, $C_6H_7O_{11}N_3$ ($\rho = 1.6$ g/cm^3) for thicknesses < 1 μm and Makrofol, $C_{16}O_3H_{14}$ ($\rho = 1.2$ g/cm^3) for thicknesses > 1 μm]. The thickness ranged from 0.1 to 20 μm and was measured interferometrically.[28] The foils were spanned over plane metallic target holders with open holes 5 mm in diameter. In most cases the foils covering the 5-mm hole entirely were large compared with the laser spot size. For high-speed photography we also used 400—1000-μm-wide foil strips.

In Fig. 2 the various diagnostics used are shown: a calorimeter behind the target which intercepts the accelerated foil material, a high-speed photographic system using 10-ps dye-laser pulses and an integrating sphere (Ulbricht sphere) for laser-light absorption measurements. In addition, optical detectors for measuring the scattered and transmitted laser light, ion Faraday cups, a Thomson parabola mass spectrometer, x-ray pinhole cameras, a flat crystal Bragg spectrometer and a multichannel absorbing foil spectrometer for the x-ray continuum were used (not shown in Fig. 2). Details of these diagnostics are described in the following sections.

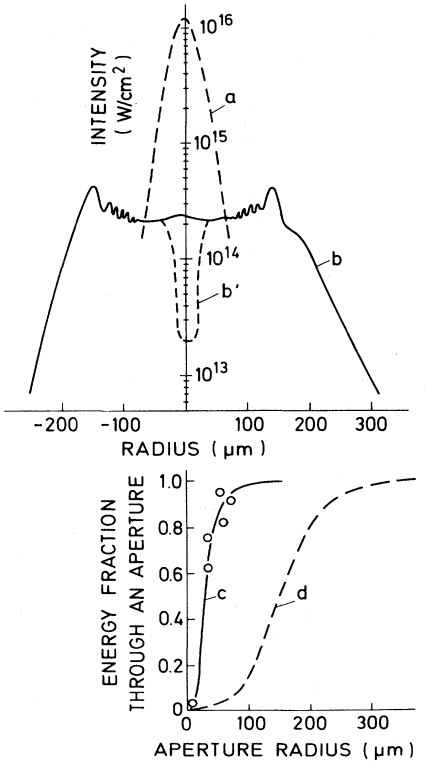

FIG. 4. Radial intensity distribution on target (curves *a* and *b*) and the energy fraction transmitted through an aperture (curves *c* and *d*) in focus (*a* and *c*) and 1 mm out of focus (*b* and *d*). Incident energy was 100 J. Curves *a* and *d* are calculated from the directly measured curves *b* and *c*. (Calculating curve *a* from curve *c* we assumed a smooth dependence of the intensity on radius; for the integration of curve *d* from *b* the modulation due to interference fringes was omitted.)

III. EXPERIMENTAL RESULTS

A. Reflection and transmission of laser light

For measurement of the overall reflection losses into the total solid angle the target was placed in the center of an Ulbricht sphere 30 cm in diameter.[29] The incident laser light entered the sphere through a hole 7 cm in diameter. Its inner surface was coated with Kodak white reflectance paint. The infrared $\lambda = 1.3$-μm laser light was measured with time-integrating germanium diodes. For calibration purposes the laser pulse was fired into the sphere when the target was removed from the center. The incident light then hits the rear inner surface of the Ulbricht sphere. To avoid errors caused by plasma production and damage to the white reflectance paint the intensity of the light at the wall of the sphere had to be kept below 2 GW/cm^2. In addition to the losses into the Ulbricht sphere, the reflection into the focusing lens was measured as schematically shown in Fig. 2.

The reflection losses at the target, in general, depend on irradiation conditions such as intensity, spot size, angle of incidence, and polarization. For the parameter used in this experiment the measured total reflection losses are plotted in Fig. 5. The measurement was made with a 2-μm-thick foil target, which is thicker than the ablated layer thickness and which, therefore, shows no transmission of laser light. The reflectivity increases from 25% at 10^{12} W/cm^2 to about 60% at intensities $\geq 10^{15}$ W/cm^2. In the high-intensity range the reflectivity shows a tendency to decrease slightly.

To complete these data, we also show examples of the angular distribution of the reflected laser radiation. The distributions shown in Fig. 6 for different spot sizes and intensities are measured with Ge diodes surrounding the

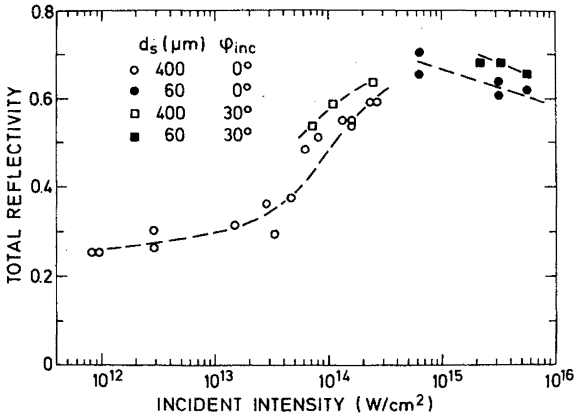

FIG. 5. Reflectivity as a function of incident intensity. With $\varphi_{inc}=30°$ the incident light was s polarized.

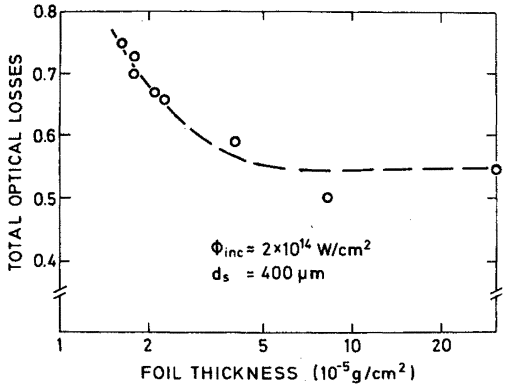

FIG. 7. Total optical losses (reflection plus transmission) measured with an Ulbricht sphere as a function of the plastic foil thickness.

target in the plane perpendicular to the electric field vector of the incident light. The horizontal bars (0°—14°) represent the amount of energy reflected through the focusing lens, which only accepts some fraction of the total reflection losses. With a spot 400 μm in diameter and intensities of around 10^{14} W/cm^2, we observe enhanced side-scattering, often with an indication of a peak at angles of 60° to 70° to the laser axis. As observed on burn paper surrounding the target, the scattered radiation was not axisymmetric, side-scattering peaks appearing only in the plane perpendicular to the E field of the incident laser light.

A more detailed discussion of the interesting physics underlying these observations would exceed the scope of this paper. We like to mention only a few points. The reflectivity depends on different processes such as classical absorption, resonance absorption at the critical layer, and stimulated Brillouin losses. With increasing intensity the electron temperature increases and collisional absorption becomes less effective, leading to an increase in reflectivity, as observed. In addition, losses due to stimulated Brillouin scattering are important. Under our experimental conditions we identified in a separate experiment stimulated Brillouin losses when the intensity was raised above $\sim 10^{13}$ W/cm^2.[30] Also, the observed enhanced side-scattering may be due to stimulated Brillouin side-scattering.

If the foil thickness is decreased below the ablated depth, the irradiated foil becomes underdense as a result of expansion, so that laser light is transmitted.[20,31] The total optical losses into 4π (reflection plus transmission) were measured with the Ulbricht sphere (see Fig. 7). They increase as a result of transmission if the foil is thinner than about 3×10^{-5} g/cm^2 ($\hat{=}$0.2-μm Zapon foil) at 2×10^{14} W/cm^2. Consistent with this type of measurement are directly measured values of the light transmitted into the rear solid angle 2π as plotted in Fig. 8. The foils become transparent at a thickness below $(2-3)\times10^{-5}$ g/cm^2 ($\hat{=}$0.1—0.2 μm Zapon foil) at 2×10^{14} W/cm^2 and below $(6-8)\times10^{-5}$ g/cm^2 ($\hat{=}$0.4 μm Zapon foil) at 3×10^{15} W/cm^2. These thicknesses are well correlated with the ablation depth given in Sec. III C.

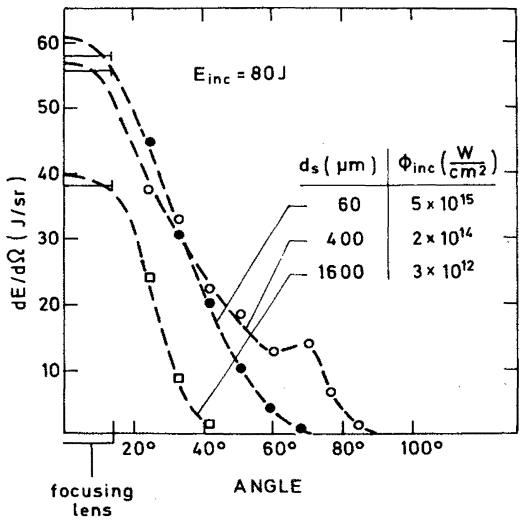

FIG. 6. Angular distributions of reflected light at different spot sizes but at the same incident energy (plotted vs an angle measured with respect to the axis of the incident beam in the plane perpendicular to the E vector of the laser light).

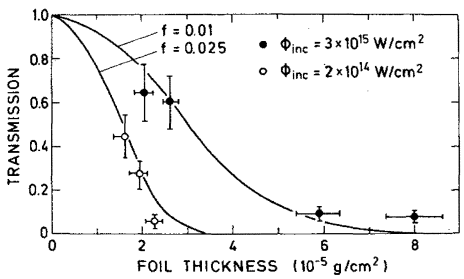

FIG. 8. Transmission of laser light through thin foil targets. Solid curves represent hydrodynamic code calculations, see Sec. IV.

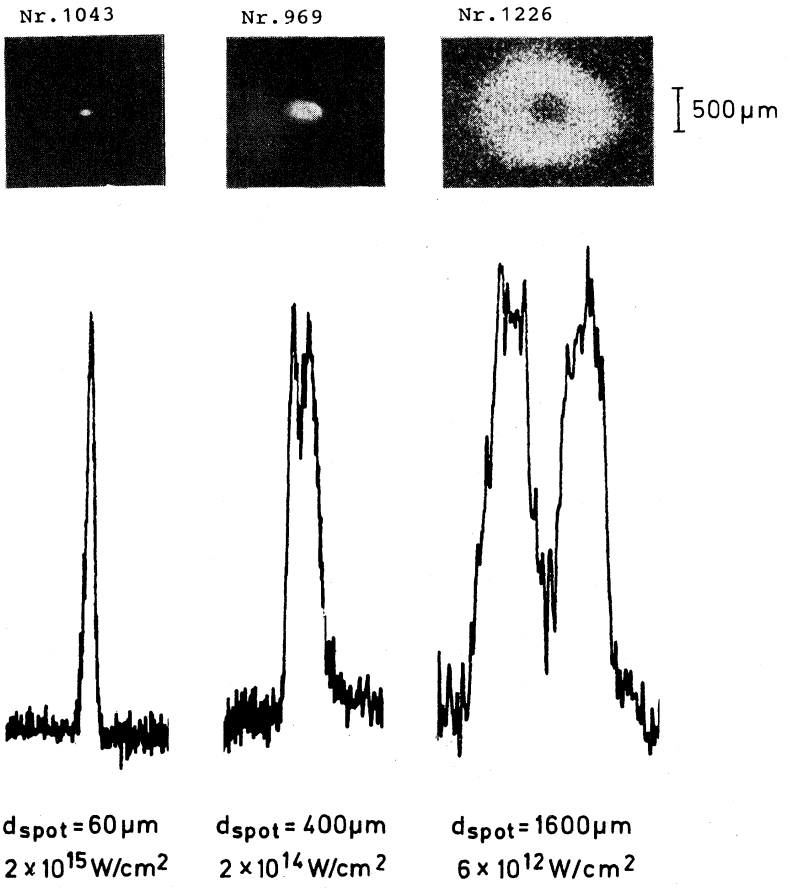

FIG. 9. X-ray pinhole pictures at different spot sizes (observed at 45° to the laser axis from the front side, 12-μm pinhole, 25-μm Be as filter).

B. X-ray and ion measurements

1. X-ray continuum

The laser plasma generated on the irradiated foils was studied by x-ray and ion diagnostics. Figure 9 shows pinhole photographs at photon energies $h\nu \geqq 1$ keV taken at different optical spot sizes from 60 μm (target in focus) to 1600 μm. It is observed for the conditions of this experiment that the size of the x-ray-emitting hot plasma is approximately equal to the optical spot size. Within the spatial resolution ($\cong 15$ μm) the pinhole pictures look fairly homogeneous; we did not observe a pronounced structure. The reduced luminosity observed in the center when the target is out of focus corresponds to a reduced optical intensity caused by the focusing lens with a center hole.

For space- and time-integrated measurement of the x-ray continuum, absorbing foil scintillator combinations with photomultipliers as detector were used. The detectors view the target at an angle of about 45° to the laser axis. Any direct fast electrons emitted from the plasma were kept away from the detectors by magnetic fields. The calculated spectral response of the different detector channels is shown in Fig. 10. The low-frequency cutoff is caused by the metallic-foil entrance window, the high-energy cutoff by the finitely thick scintillator,[32,33] which does not absorb high-energy photons. For the scintillator itself we assumed a conversion efficiency of x-ray photon energy into visible light independent of the photon energy $h\nu$.[33] This was also assumed for $h\nu < 1.5$ keV, in which spectral range no measured data are reported, to our knowledge. To remove this uncertainty in the low-energy

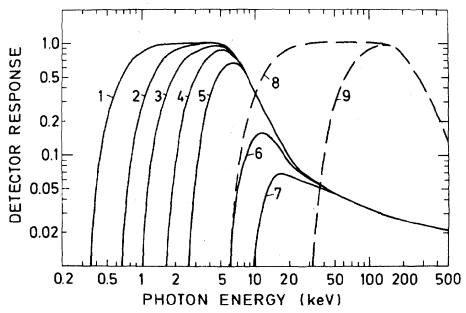

FIG. 10. Spectral response of the x-ray detector used. Channels 1–7: 0.2-cm plastic scintillator (Nuclear Enterprises NE-102-A) with 2-μm Be, 12.5-μm Be, 50-μm Be, 200-μm Be, 800-μm Be, 150-μm Al, and 500-μm Al foil. Channels 8 and 9: 1.6-cm NaI scintillator with 150-μm Al and 500-μm Cu foil.

region, x-ray Si diodes with 2- and 12.5-μm Be windows were also used instead of the scintillators in some shots. The detectors were absolutely calibrated by comparison with a calibrated calorimeter with an absorbing foil as entrance window for x radiation and with the laser plasma itself as source.

Typical measured spectra are shown in Fig. 11. In Fig. 11(a) the energy per steradian absorbed in the scintillators is plotted as a function of the detector low-energy $1/e$ cutoff. The data points are mean values of a larger series of 30—40 shots. Figure 11 shows a strong increase of hard-x-ray emission with increasing laser intensity, indicating an enhanced production rate for hot electrons. The measured data points of Fig. 11(a) are related to the emitted spectrum $d^2E/d\Omega\, d(h\nu)$ by

$$\frac{dE}{d\Omega} = \int \frac{d^2E}{d\Omega\, d(h\nu)} R(h\nu) d(h\nu)$$

with $R(h\nu)$ the detector response shown in Fig. 10. A fit is obtained by assuming a two-temperature spectrum consisting of a cold (T_c) and a hot (T_h) component:

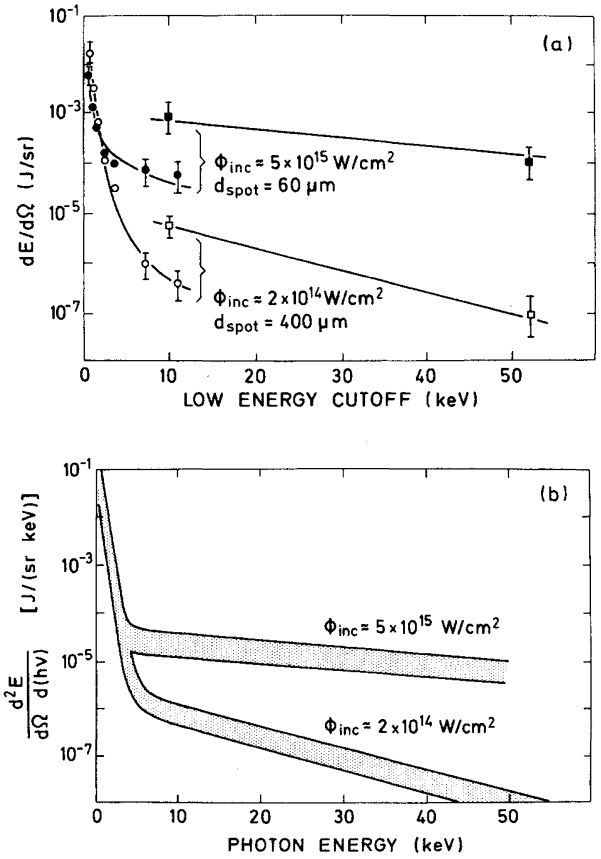

FIG. 11. Measured x-ray continuum. (a) Detector signals (energy absorbed by the scintillator) vs low-energy cutoff. ● and ○: NE-102-A. ■ and □: NaI scintillator. The NaI data points are above the NE-102-A data points owing to the enhanced response of the thick NaI detectors; see Fig. 10. The solid lines are optimum fits using Eq. (2) for the x-ray spectrum. (b) Spectra according to Eq. (2) consistent with the measurement in Fig. 10(a).

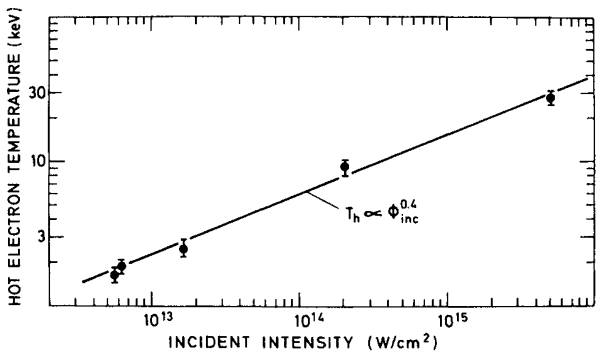

FIG. 12. Hot-electron temperature as a function of the incident intensity.

$$\frac{d^2E}{d\Omega\, d(h\nu)} = a_c e^{-h\nu/kT_c} + a_h e^{-h\nu/kT_h} . \quad (2)$$

Spectra of this type consistent with the data of Fig. 11(a) are shown in Fig. 11(b). The corresponding values for T_c and T_h are given in Table I. The measured scaling of the hot-electron temperature with intensity ($T_h \propto \phi_{\text{inc}}^{0.4}$) is plotted in Fig. 12.

The spectra shown in Fig. 11 are characteristic of foils thicker than 1 μm. With very thin foils, the x-ray emission decreases as shown in Fig. 13. The decrease in x-ray emission sets in at similar thicknesses for which the foil becomes transparent for the laser light (Fig. 8). Such behavior is expected because thin foils are no longer heated by the laser when they become underdense and consequently less radiation is emitted.

From the integrated hard-x-ray energy ($E_{\text{x ray}}$) the total energy contained in hot electrons (E_{el}) was estimated.[34] For an isotropic hard-x-ray emission Eq. (2) yields $E_{\text{x ray}} = 2\pi a_h k T_h$. The numbers for $E_{\text{x ray}}$ given in Table I are characteristic of foils thicker than 2 μm up to solid targets a few mm thick. A thick-target model thus seems

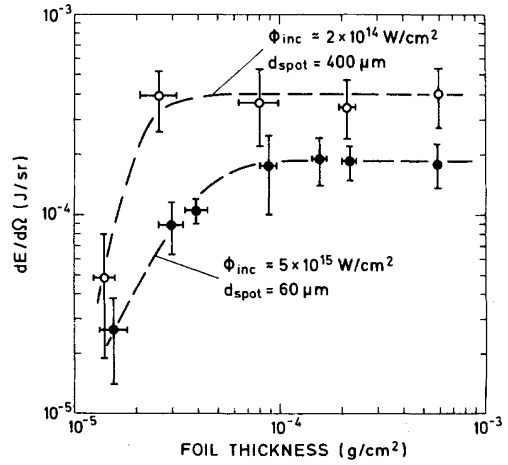

FIG. 13. X-ray continuum radiation measured (channel 2 in Fig. 10) as a function of the target thickness.

TABLE I. Electron temperature and total electron energy obtained from Fig. 10.

ϕ_{inc} (W/cm^2)	kT_c (keV)	kT_h (keV)	$E_{x\ ray}$ (J)	E_{el} (J)	E_{abs} (J)
2×10^{14}	0.3–0.4	8–10	$\sim10^{-5}$	2–3	40
5×10^{15}	0.3	25–30	$\sim5\times10^{-3}$	25–40	35

to be appropriate for generating the hard x rays as a consequence of the interaction of the hot electrons with the target material. [The observation that foils even thinner than the range of hot electrons (~10 μm) did not change the hard-x-ray emission may be attributed to strong electrostatic fields, which prevent the electrons from leaving the target region; see also the last paragraph of Sec. III B 2 b.] Using the formulas for the thick-target case worked out in Ref. 35, we find for E_{el} the values given in Table I. Although this method has to be considered as a rough estimate, it shows the trend that the energy transfered to hot electrons becomes, at high intensities ($\geq10^{15}$ W/cm^2), comparable with the absorbed laser energy E_{abs}, whereas, at lower intensities ($\leq10^{14}$ W/cm^2), it is only a small fraction of E_{abs}.

2. *Ion velocity spectra*

a. Diagnostic techniques. The velocity distribution of the ions in the expanding plasma was measured with time-of-flight (TOF) detectors and a Thomson parabola (TP). The detectors were positioned around the foil target to measure the angular distribution of the expanding plasma at the front and rear side, as shown in Fig. 14(a). It is already noted at this point that we found ion diagnostics suitable for studying features of the fast-ion expansion at high intensities. It was found, however, that they are less suited to determining quantities characterizing the foil acceleration process such as the velocity of the accelerated foil or the total ablated mass. This is because strong recombination occurring during plasma expansion[36,37] renders interpretation more difficult, as described in detail below.

The design of the TOF detectors [Fig. 14(b)] was similar to that described in Ref. 38. Secondary electron contributions to the ion current were minimized by a honeycomblike collector structure which recaptures, in part, the emitted secondary electrons and by a retarding electric field generated by a cylindrical electrode. Plasma electrons were separated from the ions by a fine entrance grid with a mesh size (50 μm) of the order of the plasma Debye length. To keep the plasma density at the detector low (i.e., the Debye length large) and to improve resolution of the velocity of the fastest ions, a large distance (140 cm) between the detector and plasma was used.

Typical TOF signals are shown in Figs. 14(c) and 14(d). Figure 14(c) illustrates the increase in ion velocity if the intensity is increased from 2×10^{14} to 5×10^{15} W/cm^2. As another example, Fig. 14(d) compares the front and rear signals of a 1.8-μm-thick foil irradiated with 2×10^{14} W/cm^2. A back-front asymmetry is evident. The ion velocity taken at the peak of the ion current is 1.5×10^7 cm/s at the rear side, but 6×10^7 cm/s at the front side.

A quantitative analysis of the TOF signals requires a knowledge of the charge state Z of the ions. For this purpose one of the detectors [C or E in Fig. 14(a)] was replaced by a Thomson parabola spectrometer, which allows the different ion species in the expanding plasma to be separated. The ions entered the parallel magnetic and electric fields (typically 1 kG and 1 kV/cm) through a 300-μm pinhole at a distance of 50 cm from the target. The ion parabolas were recorded on cellulose nitrate film, which is suitable for quantitative analysis by counting the holes or craters due to individual ions under the microscope. To avoid charge exchange between plasma ions and the ambient gas atoms the pressure in the target chamber and in the Thomson parabola housing was kept below 10^{-5} Torr.

Typical Thomson parabolas are shown in Fig. 14(e). The dominance of highly ionized species is evident. Values for the velocity spectrum are shown in Fig. 14(f). At the highest velocities $\geq7\times10^8$ cm/s we observe mainly protons,[39] which is expected if the protons (with $A_H/Z_H=1$) are accelerated by the same electric potential as the heavier species (with $A/Z\cong2$).

Figure 14(f) also shows a comparison of the TP data with the velocity spectrum obtained from TOF measurements. To calculate the velocity distribution from the TOF signal, an assumption on the average Z has to be made. Figure 14(f) shows that $Z=5$ (solid line) seems to be appropriate for the velocity range $10^8\leq v\leq5\times10^8$ cm/s and $Z=1$ (dashed line) for the highest velocities ($v\geq5\times10^8$ cm/s). The shape of the ion velocity distribution in Fig. 14(f) is characteristic of isothermal expansion of a plasma consisting of a cold and a hot component.[40]

If the charge state Z of the ions is known, quantities like the total mass and the energy of the ablated plasma or the momentum and energy transfered to the foil can be determined from TOF measurements. A major contribution to these quantities stems from the slow ions ($v\leq10^8$ cm/s), which are expected to undergo strong electron recombination during expansion. Experimental evidence of the occurrence of such recombination is available: We find agreement between the energy obtained from TOF data and the totally absorbed energy (Sec. III A) only if an average $Z<5$ is assumed for the cold component. Especially the relatively cold accelerated foil material moving to the rear side seems to arrive at the TOF detectors to a large extent as neutral matter with an average $Z\ll1$. This results from a comparison of the TOF data with the calorimetrically measured energy of the accelerated foil (see Sec. III C).

Strong recombination effects are also theoretically predicted by an average-Z model similar to that presented in Ref. 36, which we have applied for the conditions of this experiment. In particular, recombination is effective

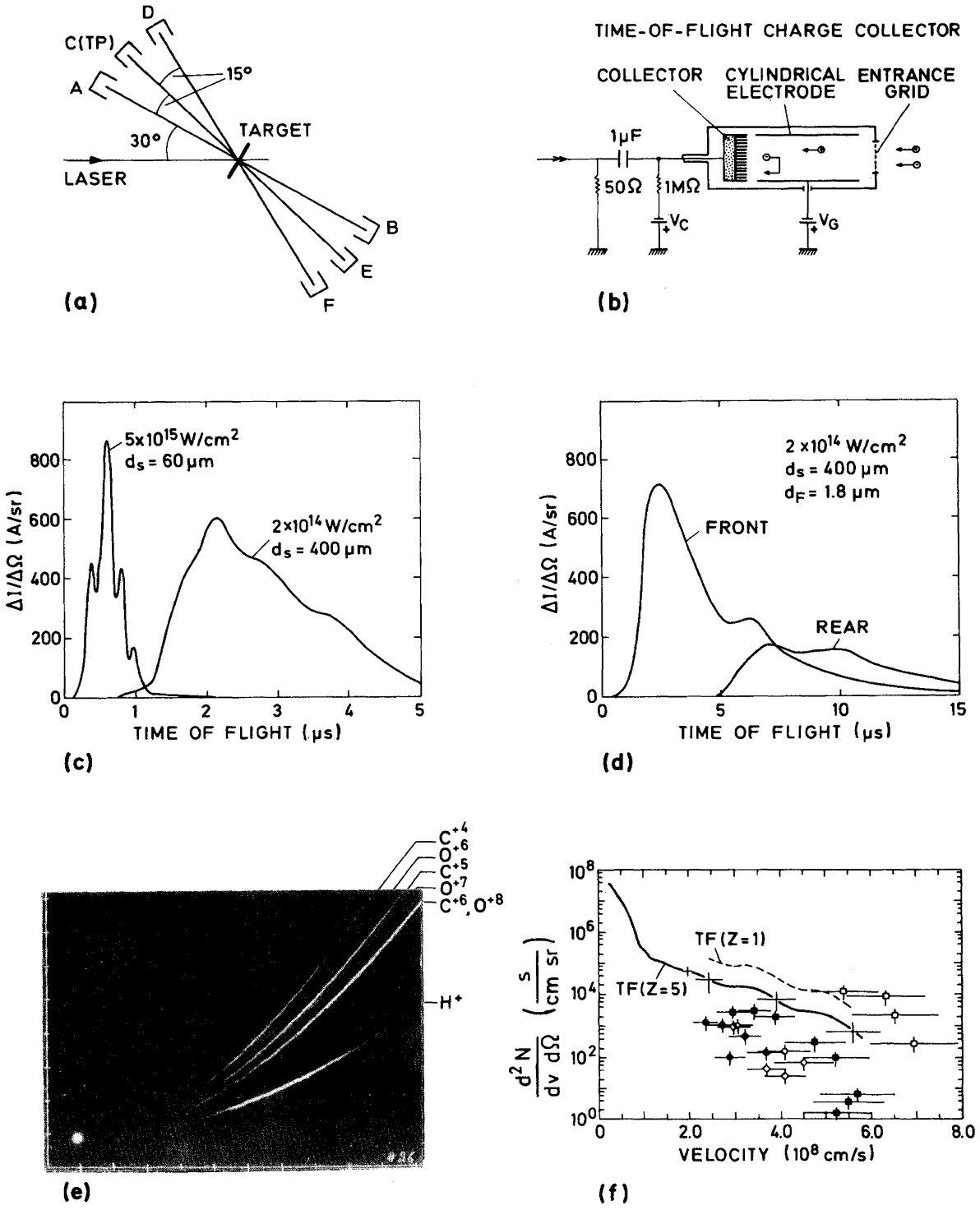

FIG. 14. Ion diagnostics. (a) Arrangement of detectors around the target. (b) Setup of a TOF detector. (c) TOF signal at different intensities (front collector A). (d) TOF signal at front and rear side (collectors A and B), $d_F = 1.8$ μm, $\phi_{inc} = 2\times10^{14}$ W/cm^2. (e) Thomson parabolas recorded on cellulose nitrate film (4×10^{15} W/cm^2). (f) Ion velocity distribution from TOF [curves TF($Z=1$) and TF ($Z=5$)] and TP (□, H^{1+}; ■, O^{8+}, N^{7+}, C^{6+}; ○, O^{7+}; ●, O^{6+}; ◇, N^{6+}; ◇, N^{5+}) (4×10^{15} W/cm^2).

if the expansion starts from a dense and cool initial state of the plasma, as is the case for the slow ions.

b. Fast-ion studies. Owing to the recombination problem no further conclusions have been drawn from slow ions. More reliable information can be derived from fast ions. We have already presented these fast-ion studies at high laser intensities in detail in Ref. 23. Here we summarize only the most essential points.

Figure 15 shows ion velocity spectra measured by collectors *A* and *B* [Fig. 14(a)] at the front and rear side of the target at different foil thicknesses. Each point is obtained by averaging up to ten laser shots under identical conditions. The spectra are symmetric with thin foils. With increasing foil thickness they become strongly asymmetric. The transition occurs at the same foil thickness (0.3—1 μm) at which transmission of the laser light sets in

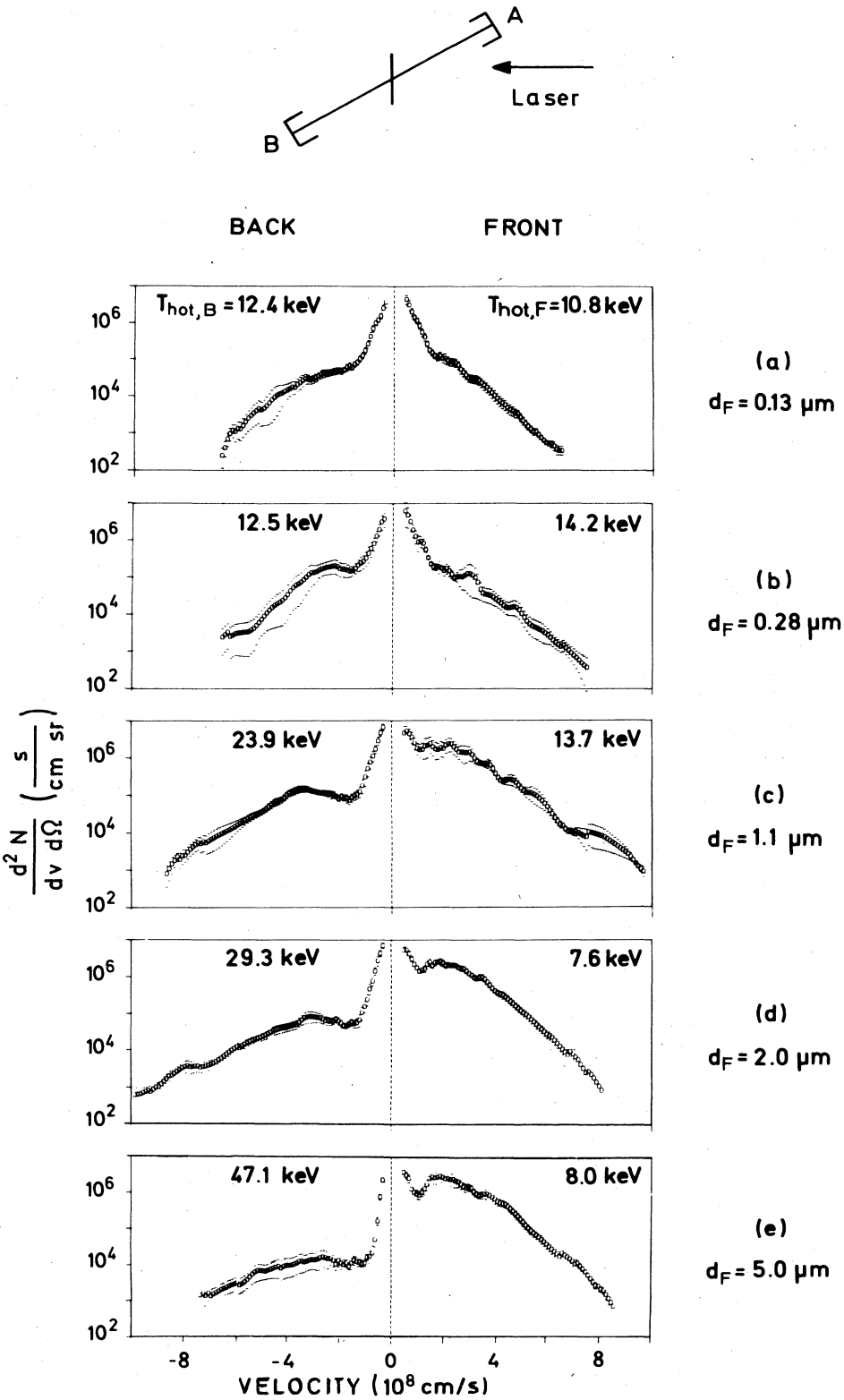

FIG. 15. Ion velocity distribution at front and rear sides at different foil thicknesses. $\phi_{inc} \cong 4 \times 10^{15}$ W/cm^2.

and the x-ray emission from the target decreases (Figs. 8 and 13). This thickness range corresponds to the ablated depth (Sec. III C). With increasing foil thickness the number of fast ions at the rear side is more and more reduced and at 10 μm fast ions were below the detection limit. Figure 15 also gives values for the hot-electron temperature as determined by an isothermal expansion model applied to the high-velocity tail of the spectrum.[40] T_h at the front side shows no systematic variation, its mean value being 11 keV. At the rear side a systematic increase of T_h up to nearly 50 keV is observed with increasing foil thickness.

The measurement in Fig. 15 was made in the direction of the target normal. To obtain values for the total losses of fast ions, we also measured the angular distribution. Typically, the ions are emitted in a very directional pattern around the laser axis. A characteristic value for the total energy of fast ions at high irradiance ($\cong 3\times 10^{15}$ W/cm^2) is 20—30 % of the absorbed energy. This value is characteristic of foils thicker than the ablated depth when the ions are preferentially emitted at the front side. The fractional fast-ion loss strongly decreases as the intensity. At 10^{14} W/cm^2 it was near the detection limit ($\leq 1\%$).

These data were analyzed to find out in what way the electron energy is deposited in the target material. We first note that the fast-ion energy measured at the rear side cannot be attributed to electrons orbiting from the front side around the target to the rear side,[41] because we used a target of large area. It is therefore assumed that the hot electrons penetrate the foil and create at the rear side a hot plasma which expands and causes the observed fast-ion emission at the rear side.

One may consider the following simple model. The hot electrons heated by the laser at the front side are reflected at the outer plasma boundary and then penetrate the foil. In this way only a small energy fraction [of the order $(Zm_e/m_i)^{1/2}$, $m_{e,i}$ represents electron and ion mass] would be used for ion acceleration,[42,43] whereas most of the energy would be deposited in the dense target resulting in preheat. Foils thinner than the electron range should explode symmetrically (exploding pusherlike behavior).

This, however, was not observed experimentally. The transition from symmetric to asymmetric rear front ion expansion already occurs at a foil thickness below 1 μm, which is less than the expected electron range. (We calculate for $T_h = 11$ keV, according to the ion data, a range of $\cong 3$ μm, and for $T_h = 25$—30 keV, according to the hard-x-ray continuum, a range of $\cong 15$ μm in the plastic foil; a more detailed analysis is given in Ref. 23.) It is thus concluded from the bilateral fast-ion blowoff that the hot-electron energy deposition is a more complex process not consistent with the simple model based on an uninhibited hot-electron flux into the target given above. This evidence was confirmed by x-ray spectroscopic diagnostics applied in this experiment. The $K\alpha$ emission from the dense cold target material below the spot was measured and analyzed.[25] The hot-electron energy consistent with the $K\alpha$ emission was only 3% of the absorbed energy.

If the hot-electron energy is not deposited in the dense target, other energy channels must exist. One is the production of fast ions. The measured fractional fast ion energy loss being 20—30 % is much higher than $(Zm_e/m_i)^{1/2} \cong 2\%$ as expected for an uninhibited electron flow into the target. Another energy channel may be lateral energy flow: instead of depositing energy inside the target below the spot the electrons may move laterally and deposit their energy far from the irradiated spot. Experimental studies of such lateral effects are given in Sec. III D 1.

Finally, we compare the fast-ion measurements to the x-ray measurements of Sec. III B 1. Both the hard-x-ray emission and the fast-ion generation are correlated, since they are both strongly intensity dependent and only become important at high intensities above $\cong 10^{15}$ W/cm^2. An interesting point concerns the estimation of the total hot-electron energy. Certainly the thick-target model used in Sec. III B 1 has to be modified if the hot-electron flux into the dense target is inhibited and the electrons stay in the ablated plasma. Although a detailed analysis of this problem is very complicated, the following consideration is given as a justification for the thick-target model used for estimating the hot-electron energy: What counts for the x-ray production by electron-ion (two-body) collisions is the product of the ion density ρ and the electron path length ($\int \rho\, dx$), which is roughly estimated in the following way. If the electrons are prevented from entering the dense target, they have to pass the ablated plasma many times. The number of reflections at the outer plasma boundary is roughly given by the ratio of the measured fractional fast-ion loss (0.2—0.3) and the energy coupled into fast ions per reflection $[\cong (Zm_e/m_i)^{1/2} \cong 0.02]$, which is 10—15. In the range 10^{15} W/cm^2 the ablated depth ρd_a is $\sim 10^{-4}$ g/cm^2 (see Sec. III C), and thus one obtains $\int \rho\, dx \cong (10\text{—}15)\rho d_a \cong 10^{-3}$ g/cm^2. This value is comparable with the electron range, and so sufficient electron-ion collisions generating hard-x-ray emission can occur.

C. Energy transfer and ablation

The energy transfered to the accelerated foil was measured by a plasma calorimeter positioned at the rear side of the foil, which is shown in Fig. 16. The accelerated and heated foil material is captured by a conically shaped calorimeter [commercial type: Compagnie industrielle des Lasers (CILAS), 64], creating a temperature rise in the calorimeter wall (1-mm-thick graphite), which is measured by thermocouples.

It is important to avoid errors due to incomplete ab-

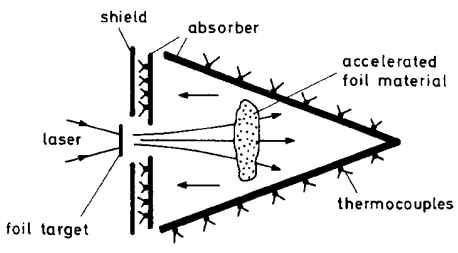

FIG. 16. Scheme of the calorimeter configuration used to measure the foil energy.

sorption of the energy contained in the foil material by the calorimeter wall. We tested such energy reflection effects with a plane calorimeter as often used for plasma ion calorimetry.[44] With a second calorimeter opposite this calorimeter we measured considerable energy reflection losses. For example, an accelerated 10-μm foil impinging on the calorimeter surface (aluminum) showed 40% energy reflection. We attribute this energy reflection to backscattering of foil material from the calorimeter wall. In this process gas dynamic effects caused by vaporized foil material or direct reflection of molecules or atoms[45] may be important. (Radiation losses from the heated wall are negligible under the conditions here.)

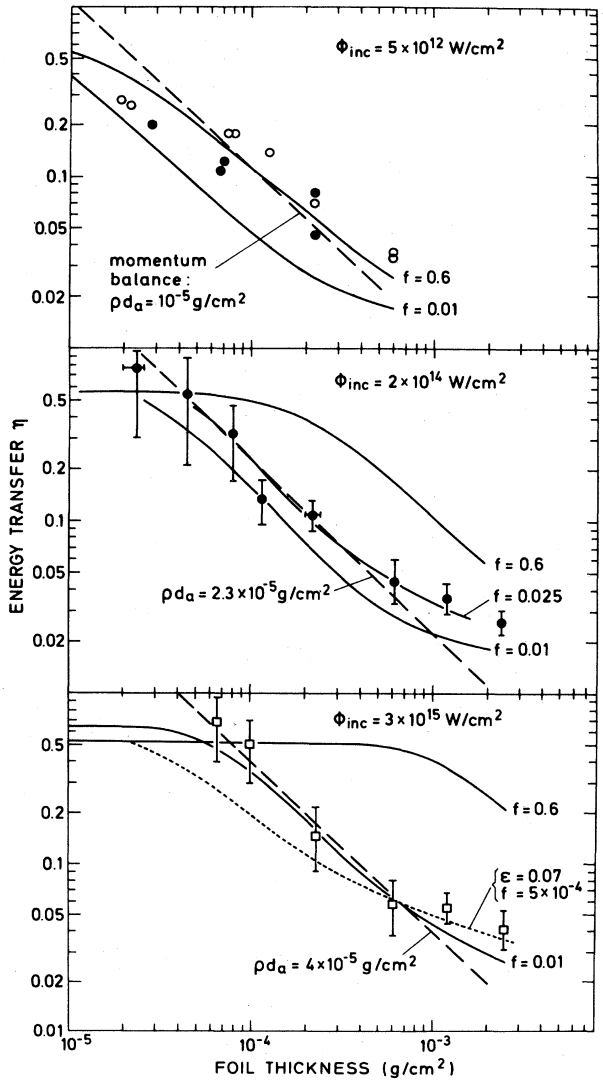

FIG. 17. Energy transfer to the accelerated foil material (η) measured by calorimeter plotted vs foil thickness for different intensities. □, 60-μm; ●, 400-μm; ○, 1600-μm laser spot diameter. Dashed line: fit using the momentum balance equation (1) to obtain the ablated depth d_a. Solid lines: hydrodynamic-code results for different f values. Dotted line: hydrodynamic-code result assuming 7% preheating. The hydrodynamic-code results are described in Sec. IV.

We therefore used the closed configuration shown in Fig. 16. An additional calorimeter closing the entrance opening (64 mm diameter) of the conical calorimeter measures the energy reflected out of the conical calorimeter. The foil entered the calorimeter box through a hole 1 cm in diameter. The energy measured by the flat calorimeter for all the data presented below was below 5% and 20% of the energy measured by the conical calorimeter. (The surface of the flat calorimeter is 16% of that of the conical calorimeter.) As the energy of the foil, the sum of the values measured by the flat and conical calorimeters was taken.

With very thin foils, laser light is transmitted (Fig. 8), which is also measured by the calorimeter. Values for the foil energy are obtained in that case by subtracting the separately (in different shots) measured transmitted light energy.

In Figs. 17 and 18 values for the energy of the accelerated foil material measured by the calorimeter normalized to the absorbed laser energy (η) are plotted as a function of the foil thickness (d_F) and the absorbed intensity ϕ_{abs}, respectively. For thin foils (near burn-through) we find $\eta \cong 0.5$; for thicker foils η decreases as d_F^{-1}, which is understood as a consequence of the momentum balance equation (1). The observed saturation at a few percent with thick foils is related to the energy coupled into the shock wave propagating into the solid target. These processes are discussed in more detail in Sec. IV A.

The measured dependence $\eta(d_F)$ allows determination of the ablated layer depth d_a. Applying Eq. (1) ($\eta = d_a/d_F$) to the regime where the measured η is inversely proportional to d_F, we find the values for d_a given in Fig. 17 and plotted in Fig. 19 as a function of the intensity (open circles).

The ablated layer depth was also determined in this experiment by an x-ray spectroscopy technique for comparison purposes.[15,18,46] The intensity of H- and He-like Al lines was measured with a Bragg crystal spectrometer. As targets we used in that case aluminum coated with plastic layers of different thicknesses.[47] Al lines only appear if the plastic is burned through. The ablation depth resulting from this method is also shown in Fig. 19. It is about

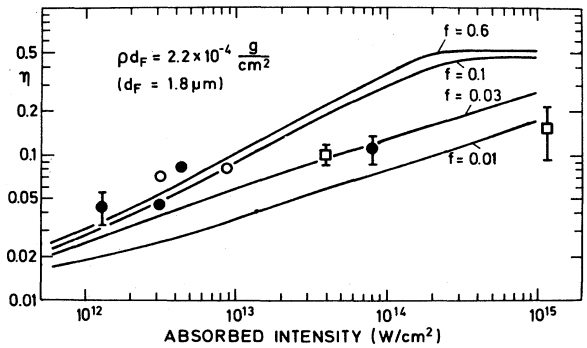

FIG. 18. Energy transfer as a function of the absorbed intensity with a fixed foil thickness. □, 60-μm; ●, 400-μm; ○, 1600-μm laser spot diameter. Solid lines are hydrodynamic-code results described in Sec. IV.

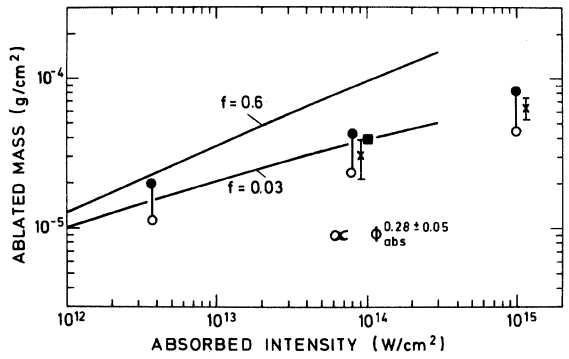

FIG. 19. Ablated mass vs absorbed intensity: ■ from x-ray line spectroscopy. ○ and ● from calorimetry [○, from simple energy balance, Eq. (1); ●, corrected values using Eq. (3) with $\gamma=2$]; ×, transmission of laser light. Solid lines are hydrodynamic-code results described in Sec. IV.

a factor of 2 larger than that determined from the calorimeter data with Eq. (1).

This discrepancy can be attributed to the application of the simplified momentum balance equation (1), which neglects two important points. (1) The angular spread of the particles due to lateral expansion reduces the total momentum of the mass moving to the front and rear side. (2) The velocity of the different mass elements is not constant, but distributed around the center-of-mass velocity. The influence of this velocity distribution has to be taken into account if the mass momentum and energy of the ablated plasma and the accelerated foil are calculated.

As shown in Appendix A, these effects can be included in a correction factor γ, and Eq. (1) has then to be replaced by

$$\eta=[1+\gamma(d_F/d_a-1)]^{-1} . \tag{3}$$

For $\gamma=1$ Eq. (3) is equivalent to Eq. (1). As discussed in Appendix A, $\gamma=2$ is a reasonable value for the experimental conditions. Values for the corrected ablation depth obtained in this way are shown in Fig. 19 and are in better agreement with the spectroscopically measured value. For comparison Fig. 19 also contains the foil thickness at which transmission sets in according to Fig. 8.

D. High-speed photography

1. Two-dimensional behavior

Shadowgrams were made by illuminating the target with a 10-ps dye-laser pulse (pulse energy $\cong 10$ μJ, $\lambda\cong 6000$ Å), as schematically shown in Fig. 2. Synchronization with the plasma-producing iodine laser was achieved by driving the mode lockers of the oscillators of both lasers with the same hf generator. The thin foil target, either a 400—1000-μm-wide strip or a large-area foil ~ 5 mm in diameter, was imaged on Polaroid film by an optics with an effective $f/10$ aperture yielding a spatial resolution of ~ 20 μm.[48]

For interpretation of the shadowgrams it is of interest to know the density n_e relating to the bright-dark interface seen in the shadowgrams. If a nonabsorbing free-electron plasma is assumed, n_e depends on the electron density gradient length L_n, the size of the plasma L along the direction of observation, and the aperture angle (φ) of the imaging lens. With $n_e \ll n^*$ (n^* is the critical density of the diagnostic laser wavelength), the observed density n_e is estimated by (compare, for example, Ref. 49)

$$n_e \cong 2(\tan\varphi) n^* \frac{L_n}{L} . \tag{4}$$

For the conditions of the shadowgrams, Fig. 20, we estimate n_e values between 10^{19} and 10^{20} cm^{-3}, assuming density gradients derived from hydrodynamic calculations.

Typical examples of shadowgrams are shown in Fig. 20. The basic processes occurring are best characterized by Figs. 20(e) and 20(f): At early times the plasma cloud created by the laser in front of the target is visible [Fig. 20(e)]. Simultaneously, the rear surface is set into motion. After a few ns [Fig. 20(f)] the expanding plasma is not visible any more and the accelerated foil material moves with high velocity to the right.

The shadowgrams in Fig. 20 are taken from shots with laser spot sizes of 1000, 400, and 60 μm in diameter. It can be seen that the lateral extent of the laser-produced plasma and the accelerated part of the foil depends on the optical spot size. At times shortly after the pulse [less than ~ 1 ns, see Figs. 20(e) and 20(h)], when the acceleration process is finished, the diameter of the accelerated foil material typically approaches the laser spot size.[50] This has been observed even for the highest intensities (5×10^{15} W/cm^2), where the lateral energy spread due to hot electrons is expected to increase. For example, in Fig. 20(h) the diameter of the accelerated part of the foil is 120 μm at 1.3 ns after the laser pulse. This corresponds to an optical spot diameter which contains 90—95 % of the laser energy (Fig. 4). At later times [Figs. 20(f) and 20(i)] the lateral size of the accelerated foil increases, which may be due to heating of the foil by the shock wave or additional preheating effects and subsequent lateral decompression.

From this observation it is concluded that the ablation pressure acts essentially in the focal spot region. However, in all shadowgrams of Fig. 20 a slow expansion of the shadow of the foils is also seen outside the focal spot region up to distances of 2 mm. An extreme example of this type is shown in Fig. 21(a), in which a 2-μm-thick foil positioned in the focus explodes over the whole field of view. It is supposed that this is caused by fast electrons that are created in the focal spot area (Sec. III B). Rough estimates based on simple hydrodynamic expansion models show that the amount of energy necessary to explain the slow expansion of remote parts of the foil is small (a few 100 mJ to a few J) compared with the total energy absorbed from the laser.

To confirm these estimates, the remote energy deposition was determined more quantitatively by using the characteristic $K\alpha$ radiation of the target material caused by the impact of fast electrons. Time-integrated $K\alpha$

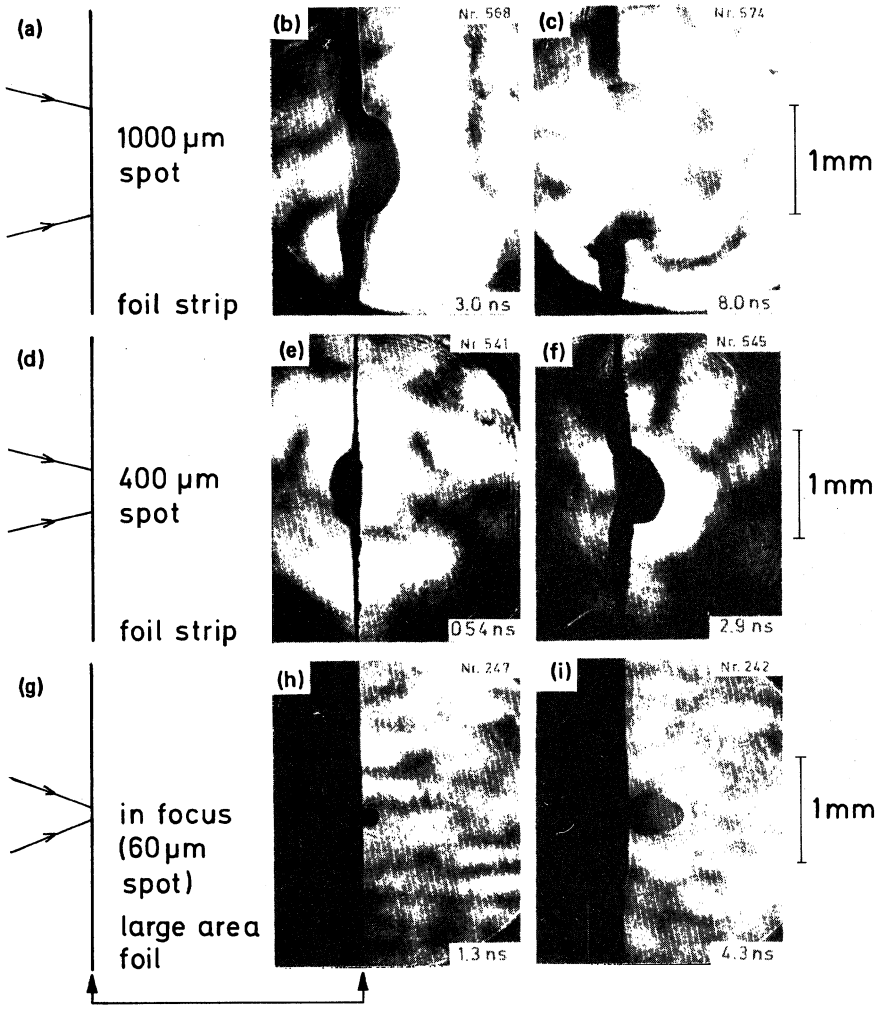

FIG. 20. Shadowgrams at different times and different spot sizes. $E_{\text{inc}} \cong 70$—100 J. Times are with respect to the maximum of the iodine laser pulse. Target: (a)—(c), 1000-μm-wide Makrofol strip, 1.8 μm thick; (d)—(f), 400—500-μm-wide Makrofol strip, 1.8 μm thick; (g)—(i), extended Makrofol foil, 20 μm thick (in this case the foil was slightly curved in order to get a sharp picture of the rear foil surface; the front side is shadowed by the foil itself and therefore not visible).

pinhole photographs of vanadium and copper targets were taken.[25] An example is shown in Fig. 21(b). A detailed analysis of the $K\alpha$ radiation shows that the remote energy deposition is caused by hot electrons of about 10 keV energy, and that the amount of energy deposited in this way is 6% of the incident energy of 100 J at intensities of about 5×10^{15} W/cm^2. An energy deposition of this type has also been found in CO_2-laser experiments, in which lateral energy losses due to the higher electron temperatures can be of major importance for the energy balance.[51]

2. *Foil velocity, acceleration, and pressure*

Each shadowgram of Fig. 20 was obtained from a separate shot. With the dye laser in quasi-cw operation (pulse duration ~ 1 μs) it was also possible to follow the target motion in one shot by streak photography (Fig. 22). The streak slit was positioned perpendicular to the foil in the center of the laser spot. At the irradiated side one observes the formation and decay of the plasma cloud. The rear foil side is accelerated during the laser pulse and reaches a constant velocity afterwards. Values of this asymptotic velocity are plotted in Fig. 23 as a function of the absorbed intensity. With a 1.8-μm-thick foil the velocity increases from 10^6 cm/s to almost 10^8 cm/s over the intensity range investigated. As expected, a 10-μm foil moves more slowly than the thinner 1.8-μm foil.

The foil velocity measured by the streak camera allows determination of the pressure P exerted by the laser-heated plasma. The equation of motion for the foil with the instantaneous mass per area M/F is given by

$$P = \frac{M}{F}\frac{dv}{dt} \cong \frac{\rho d_F v}{\tau_{\text{eff}}} \tag{5}$$

By means of Eq. (5) the pressure was determined from the

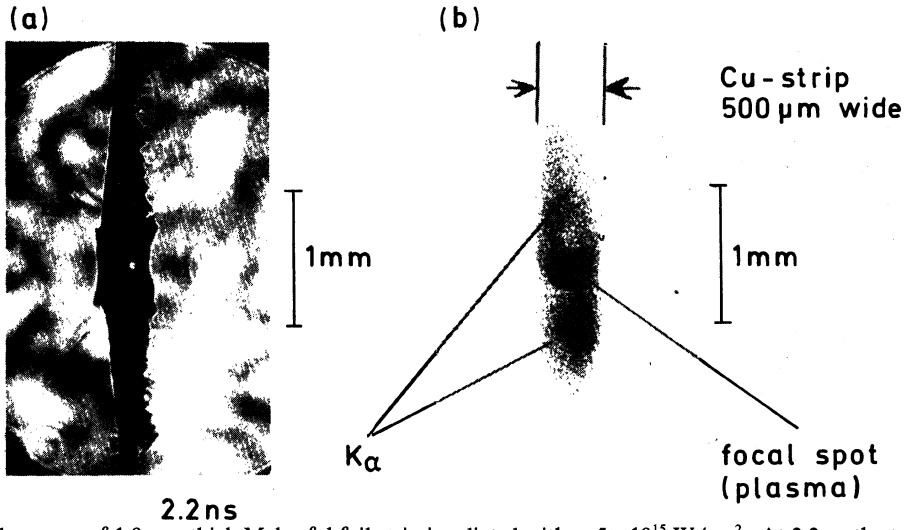

FIG. 21. (a) Shadowgram of 1.8-μm-thick Makrofol foil strip irradiated with $\cong 5\times 10^{15}$ W/cm^2. At 2.2 ns the target is seen to explode over the whole field of view. (b) $K\alpha$ pinhole picture of a 500-μm-wide Cu strip. Pinhole diameter 200 μm with 11-μm-thick Cu filter. $\phi_{\text{inc}} \cong 5\times 10^{15}$ W/cm^2.

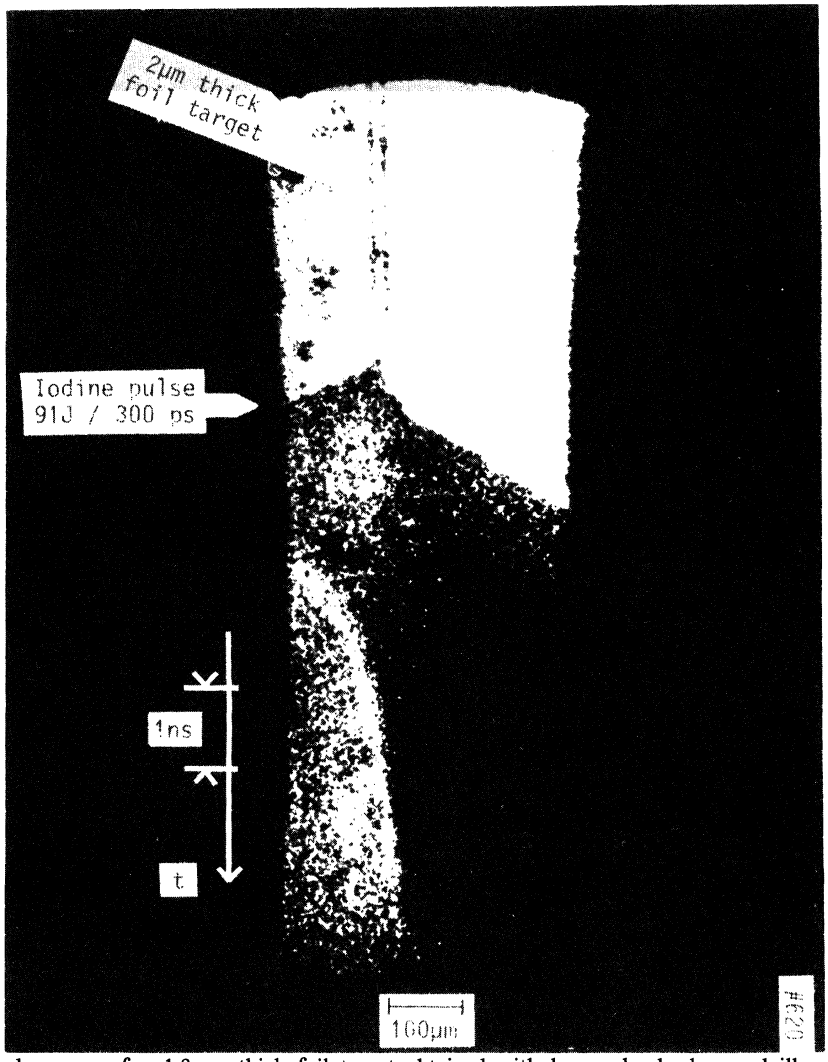

FIG. 22. Streak shadowgram of a 1.8-μm-thick foil target obtained with long-pulse background illumination. $\phi_{\text{inc}} = 2\times 10^{14}$ W/cm^2.

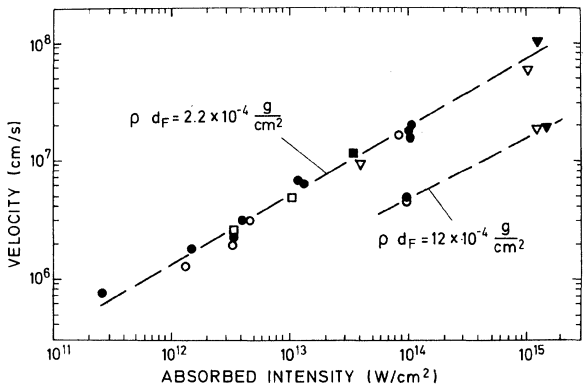

FIG. 23. Velocity of accelerated foil material plotted vs absorbed laser intensity for two different foil thicknesses: 1.8 μm ($\rho d_F = 2.2\times10^{-4}$ g/cm^2) and 10 μm ($\rho d_F = 12\times10^{-4}$ g/cm^2). ▼,●,■: streak photography with laser spot diameter of 60, 400, and 1000 μm, respectively. ▽,○,□: calculated from calorimetry for 60-, 400-, and 1600-μm spots, respectively.

high-speed photographic data, either by differentiation of the contour observed on the streak pictures or from the asymptotic velocity observed on framing photographs and an effective acceleration time ($\tau_{\text{eff}}=600$ ps as determined from the streak photographs). The mass loss of the foil during irradiation was taken into account for thin foils. The variation of pressure with intensity in shown in Fig. 24. It increases from 300 kbar at an absorbed intensity of 2.5×10^{11} W/cm^2 to 50 Mbar at 2×10^{15} W/cm^2.

These values represent upper limits of the pressure because in Eq. (5) the center-of-mass velocity (v_c) of the accelerated foil has to be used. The rear surface velocity (v_R) observed in optical shadowgraphy may be larger than v_c if the foil does not remain cold. One mechanism which may heat the foil is the shock wave propagating into the foil. The hydrodynamic calculations discussed in Sec. IV show that v_R practically coincides with v_c if the time for propagation of the shock through the foil is short compared with the laser pulse and no strong preheating mechanisms other than shock heating are dominant. The arrows plotted in Fig. 24 indicate the corrections due to the effect of foil expansion as predicted by the hydrodynamic code for an ideal-gas approximation. It is seen that this correction is of importance for the 2-μm-thick foil only at the lowest intensities. The correction may actually be less because the hydrodynamic code used an ideal instead of a real equation of state.[52]

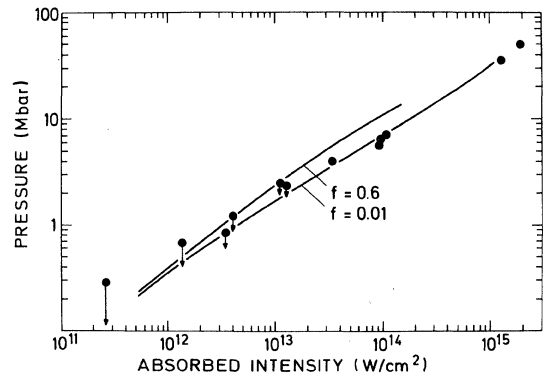

FIG. 24. Accelerating pressure as a function of absorbed intensity. Arrows indicate corrections due to expansion of the foil as described in the text.

Other preheating mechanisms than shock heating as, e.g., preheating caused by hot electrons at high intensities could increase the rear surface velocity v_R further. There is, however, also some experimental evidence that the measured v_R is close to v_c. This is done by comparing v_R as measured by optical shadowgraphy with the velocity calculated from the energy measured by the calorimeter (E_{cal}) with the equation

$$v_{\text{cal}}=\sqrt{2E_{\text{cal}}/m} \tag{6}$$

on the assumption that the accelerated foil mass m is determined by the laser spot size. This assumption is confirmed by the shadowgrams at least for incident intensities up to 2×10^{14} W/cm^2. The velocities v_{cal} determined in this way are close to the rear surface velocity v_R (Fig. 23). From the simple hydrodynamic consideration in Appendix B it follows that then v_R is not very different from the center-of-mass velocity v_c. We note that this conclusion was recently confirmed by double-foil experiments, which will be published.[50]

In addition to the foil acceleration studies we also performed experiments to observe the propagation of the shock front in transparent solid targets made of Plexiglass.[5,22] The pressures derived from these experiments confirmed the foil acceleration data. The shock experiments will be reported in detail elsewhere.

IV. NUMERICAL SIMULATIONS

A. The hydrodynamic model and its results

These experiments were interpreted by means of a one-dimensional hydrodynamic Lagrangian code, which is described in detail in Ref. 53. The code solves the hydrodynamic equations under the following assumptions. The target material is regarded as a fully ionized ideal gas with allowance for different temperatures for electrons and ions. The laser light is absorbed by inverse bremsstrahlung in the underdense corona. In addition, an arbitrary fraction of the light energy reaching the critical layer can be deposited there in order to simulate resonance absorption or other absorption processes localized at the critical layer. The absorbed energy is transported in the plasma by electrons and ions according to Spitzer's theory[54] modified by a flux limitation for the electrons which becomes important for an electron temperature gradient length comparable with the electron mean free path:

$$\vec{q}_i=-\kappa_i\vec{\nabla}T_i\ ,$$
$$\vec{q}_e=-\left[\frac{1}{\kappa_e\,|\vec{\nabla}T_e|}+\frac{1}{q_{\max}}\right]^{-1}\frac{\vec{\nabla}T_e}{|\vec{\nabla}T_e|}\ , \tag{7}$$

where $q_{e,i}$ are the energy fluxes, and $\kappa_{e,i}$ the heat conductivities[54] for the electrons and ions. The maximum electron heat flux $q_{\max}$ is conventionally written as

$$q_{\max}=fn_e kT_e\left[\frac{kT_e}{m_e}\right]^{1/2}. \tag{8}$$

The flux limiter f represents a free parameter introduced to obtain agreement between the experimental and numerical results. $f=\sqrt{2/\pi}\cong 0.8$ corresponds to the free-streaming limit of an isotropic Maxwellian electron gas. To study the influence of preheating of the dense target on the hydrodynamic behavior, the code allows for the deposition of an arbitrary fraction of the absorbed energy in the dense target. Physically, this preheating can be caused by x radiation or by hot electrons.

In Fig. 25 computer results of the foil acceleration process are shown for three different cases referred to as thin, medium, and thick foils. (The meaning of this classification will become clear later.) The incident intensity as a function of time is taken to be proportional to $\sin^2 2\pi t/\tau$ with $\tau=300$ ps, this being a good approximation to the experimental conditions. The incident peak intensity is 2×10^{14} W/cm^2 for the three cases shown. Classical absorption by inverse bremsstrahlung in the underdense plasma is only $\sim 3\%$. Of the light energy reaching the

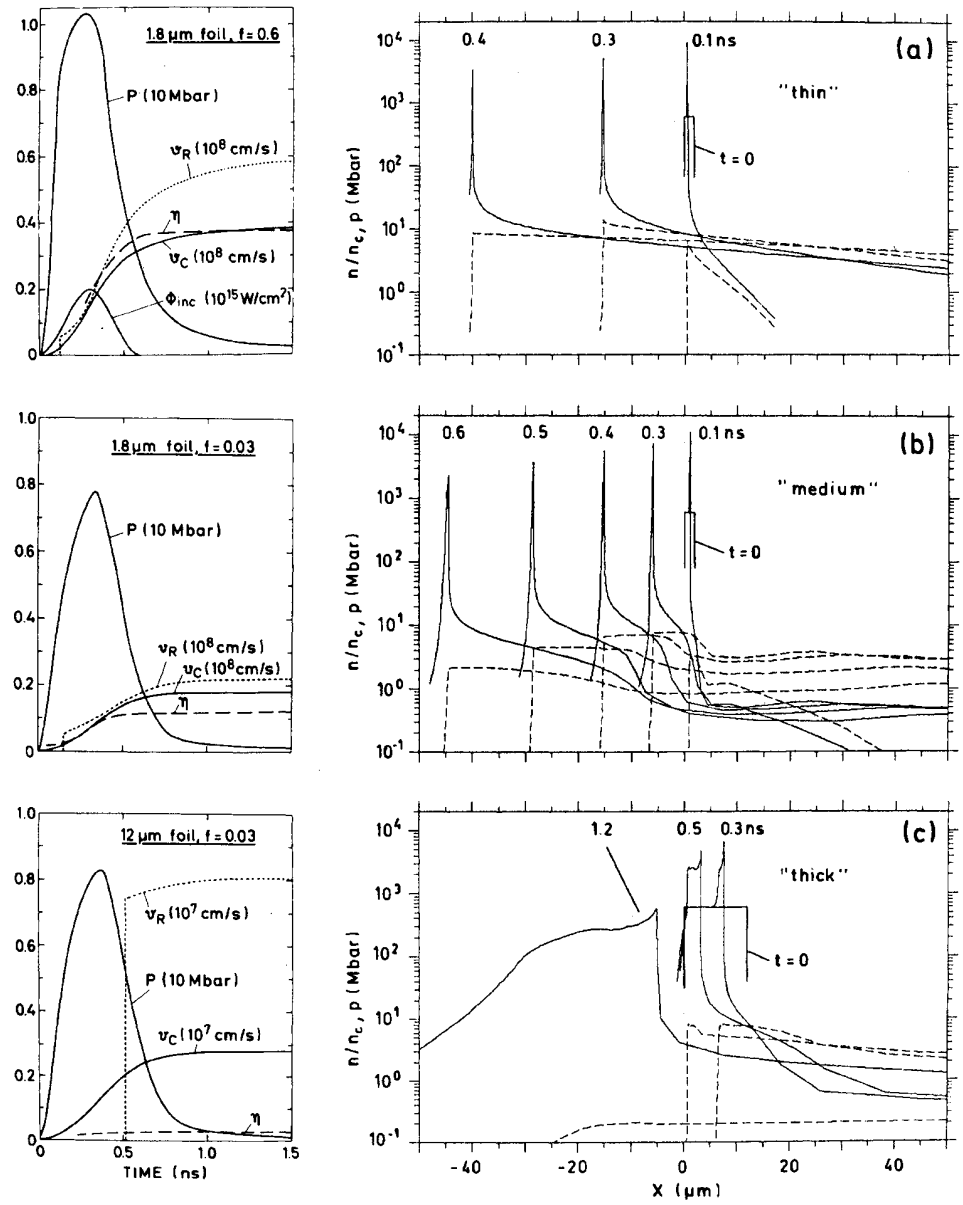

FIG. 25. Typical simulation results: spatial density (solid curves) and pressure (dashed curves) distributions at different times and temporal dependence of pressure (p), energy transfer (η), and center-of-mass (v_c) and rear side velocity (v_R). (a) 1.8-μm foil, $f=0.6$; (b) 1.8-μm foil, $f=0.03$; (c) 12-μm foil, $f=0.03$. The incident pulse, shown in (a), is the same in all cases.

critical layer 50% is deposited there, i.e., the main deposition is at $n = n_{crit}$.

We first discuss the results at "medium" foil thickness [Fig. 25(b)], which case best approximates so-called ablative acceleration. In the right-hand diagram of Fig. 25(b) a sequence of density and pressure profiles at different times is shown. At $t=0$ there is a rectangular profile of the imperturbed foil with solid density. After the laser is switched on, matter from the surface of the foil is ablated and heated to temperatures of several keV. The corresponding pressure drives a compression wave into the remaining part of the foil. Densities of up to 20 times solid-state density are reached, much higher than those expected from a single strong shock that would be created by a step laser pulse. After $t_s = 0.15$ ns the front of the compression wave—simply called shock front hereafter—has arrived at the rear surface, the whole foil is in motion and a rarefaction wave develops. Since the laser pulse is still on, the foil is further accelerated and gains kinetic energy.

In the left-hand diagram of Fig. 25(b) the time dependence of some characteristic quantities is illustrated. The ablation pressure approximately follows the laser pulse. It reaches its maximum of 8 Mbar shortly after the maximum of the laser pulse. $v_R(t)$ is the velocity of the surface of constant density $n_e = 10^{20}$ cm^{-3} and approximately corresponds to the velocity observed by our high-speed photography. The step in v_R at 0.15 ns [Fig. 25(b)] indicates the arrival of the shock front at the rear of the foil. v_c is the center-of-mass velocity of the total matter which moves to the left away from the laser. As illustrated by Fig. 26, this matter mostly consists of the cold compressed solid, but there is also a small contribution from the lower-density region close to the ablation front. Both v_R and v_c increase till the end of the laser pulse. The saturation values of the two velocities do not differ very much. Hence, the measured values for v_R are a good approximation for the center-of-mass velocity v_c at foils of medium thickness. The temperature of the compressed region (not shown in Fig. 25) increases to a few eV due to shock heating.

The energy transfer $\eta(t)$ is also shown. In correspondence to the calorimetrically determined energy transfer, it is defined as the total amount of kinetic and thermal energy of the matter that moves to the left (particle velocities <0), normalized to the absorbed energy, up to a given time t. $\eta(t)$ increases during the laser pulse time and reaches a saturation value of 12% in our case [Fig. 25(b)]. The major part of the transfered energy, 8%, is kinetic energy. The difference of 4% is thermal energy of the backward-moving, hot, ablated plasma close to the ablation layer with temperatures of a few hundred eV.

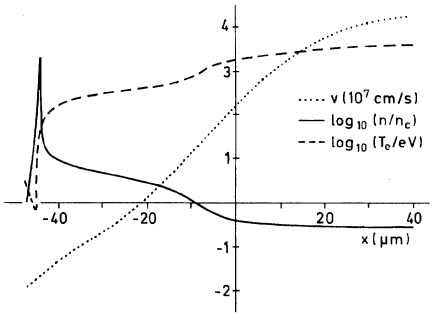

FIG. 26. Spatial density, temperature, and velocity profiles at the end of the laser pulse ($t=600$ ps) for the case of medium foil thickness [conditions as in Fig. 25(b)].

The medium-thickness range discussed so far is given if the foil is a few times thicker than the ablated depth ($d_F > d_a$) but at the same time sufficiently thin, to make the shock transition time t_s small compared with the pulse duration τ ($t_s \ll \tau$). In that case the energy of the accelerated foil is mainly kinetic energy. Different behavior is exhibited by "thin" foils with a thickness close to or less than the ablated depth ($d_F \leqq d_a$) and by "thick" foils, for which the shock front does not reach the rear side before the end of the laser pulse ($t_s \geqq \tau$).

In the example in Fig. 25(b) a flux limiter $f=0.03$ was used to treat the electron heat conduction. With $f=0.6$, but otherwise identical conditions, the ablation depth increases. The ratio $d_a/d_F = 0.5$, and the thin-foil case [Fig. 25(a)] is realized. Here 35% of the absorbed energy is transfered to the backward-flowing matter. However, most of this energy is contained in a hot plasma of relatively low density. Only 9% is kinetic energy of the compressed part of the foil. The difference between the two velocities, v_c and v_R, becomes appreciable and corrections have to be introduced if one wants to determine the ablation pressure from the measured rear-front velocity v_R.

By taking a 12-μm foil and a flux limiter $f=0.03$ the case of a thick foil [fig. 25(c)] is realized. Here the shock transition time $\tau_s = 0.5$ ns is of the same order as the pulse duration. The motion of the rear surface starts with a delay of 0.5 ns and the optically observable velocity v_R is considerably larger than the center-of-mass velocity v_c. This can be understood qualitatively as follows: From the momentum balance we see that the center-of-mass velocity is proportional to the reciprocal foil thickness $v_c \propto d_F^{-1}$. On the other hand, the velocity v_R is essentially determined by expansion of the shocked foil and is roughly proportional to the sound velocity $v_R \propto \sqrt{T}$. Since $T \propto d_F^{-1}$, it follows that the ratio $v_R/v_c \propto d_F^{1/2}$, i.e., the difference between v_R and v_c increases as the foil thickness.

The fraction of energy transfered into backward motion of matter η is calculated from the code to be 3% in the case of Fig. 25(c). The energy coupled into the shock wave η_s can be approximately determined by the formula[55]

$$\eta_s = \frac{p}{\phi_{abs}} \left[\frac{p}{\rho_0} \left[1 - \frac{\rho_0}{\rho_1} \right] \right]^{1/2} \tag{9}$$

which is valid for a stationary single shock driven by a constant pressure p. ρ_0 and ρ_1 are the densities before and behind the shock front, respectively. With the data of Fig. 25(c) we get $\eta_s = 2\%$. This value is a lower limit of η that is approached as the foil thickness further increases.

B. Comparison with experiment

In the code used the flux limiter f is introduced as a free parameter. Figure 27 shows how different measured quantities depend on f. When f is reduced below the free-streaming Maxwellian value ($f=0.8$), the ablation is less effective. Consequently, quantities correlated with the ablation such as the pressure p, the ablated depth d_a, the rear energy transfer η, and the rear surface velocity v_R decrease. In contrast, the electron temperature in the corona (taken at the maximum of the pulse) increases owing to the reduced electron heat flow. The quantities are most sensitive to variations of f in the region $f \leqq 0.1$, whereas they are almost independent of f for $f \geqq 0.1$.[56]

The circles in Fig. 27 indicate experimentally determined values. These quantities, almost all of which were measured by different methods, agree with the calculated ones in a rather narrow f-number range between 0.015 and 0.03. Even the temperature fits in this scheme if the measured hot-electron temperature ($T_{e,\mathrm{hot}}$) is identified with the maximum corona temperature calculated by the code although the hydrodynamic code only describes the electron temperature in an approximate way. It uses a single electron temperature, whereas in reality the electron distribution is locally non-Maxwellian.

For a more detailed comparison at different intensities and foil thickness we have added theoretical curves to the experimental data of Figs. 8, 17, 18, 19, and 24 for light transmission, total energy transfer η, mass ablation, and pressure. For intensities $\geqq 10^{14}$ W/cm^2 agreement is obviously only obtained with small f values $\leqq 0.03$. At lower intensities $\leqq 10^{13}$ W/cm^2 the quantities that characterize the foil acceleration are less sensitive to variations of the f value. However, it seems that f values $\geqq 0.1$ are more suitable for describing the low-intensity region. The intensity dependence of the flux inhibition is best illustrated in Figs. 17 and 18, where measured values of the energy transfer η are shown in comparison with results from the hydrodynamic code.

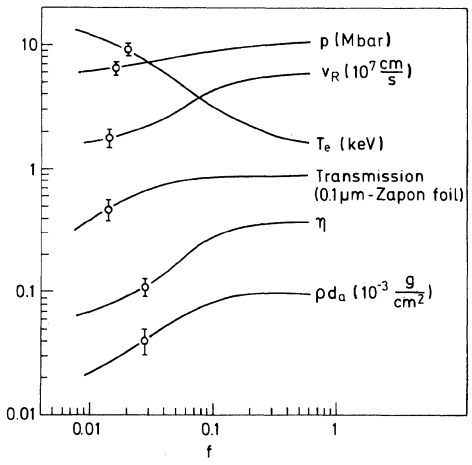

FIG. 27. Simulation of various quantities measured as a function of the flux inhibition f. Open circles represent the measured values; $\phi_{\mathrm{abs}}=10^{14}$ W/cm^2.

No special attempts were made to simulate the measured reflectivity in detail, because the code does not include processes such as stimulated Brillouin scattering or profile modifications due to light pressure effects. The experimental data of Fig. 5 are approximately consistent (fairly independent of f) with the code if it is assumed that about 50% of the light energy reaching the critical layer is deposited there. The improved absorption at intensities below 10^{13} W/cm^2 is caused by an increased contribution of inverse bremsstrahlung, which becomes important in this intensity range.

At high intensities an appreciable part of the laser energy is coupled into hot electrons, which could cause considerable preheating. For simulation of this process it was assumed that a certain fraction ϵ of the absorbed energy is deposited as preheat in the target within a range of 5×10^{-4} g/cm^2, which corresponds to 10—20-keV electrons. ϵ is chosen as a free parameter. It is found that simulations with preheating levels of a few percent are consistent with the measurements only if at the same time the f number is reduced. As an example, Fig. 17 shows at $\phi_{\mathrm{abs}}=10^{15}$ W/cm^2 a fit with $\epsilon=7\%$, in which case the f number had to be reduced to a very small value $f=5\times10^{-4}$. The same conclusion has been obtained by comparing the measured rear surface velocity v_R with simulations at different preheating levels ϵ. Examples are presented in Ref. 21. This result is further evidence of hot-electron flux inhibition as discussed in Sec. III B 2 b.

Finally, it is important to discuss some of the assumptions made in the model. One question is how accurately the one-dimensional plane calculations used approximate the process considered, which is two-dimensional because of the finite spot size. Plane-geometry models the dense foil well, if the spot size is large compared with the foil thickness, as in our case, and if we ignore processes which may occur on the scale of the foil thickness, such as foil breakup due to hydroinstabilities or local burn-through due to self-focusing, etc. The axial motion of the irradiated foil through the nonparallel focused beam, which may shift the interaction into regions of different intensities, is also of minor importance here. More relevant is the question of whether the laser-generated plasma is well approximated by the plane geometry used. If the axial extent of the plasma becomes comparable to the spot diameter, lateral effects due to lateral heat flow and the divergence of the plasma flow become important.[57]

According to Ref. 56 lateral heat flow effects are negligible if the overdense plasma layer thickness is small compared with the spot diameter. The code predicts values for the overdense layer thickness not exceeding 20 μm for $f=0.03$ and at 100 ps after the maximum of the pulse. The condition for negligible lateral heat flow is thus well satisfied for the 400-μm spots used at intensities of up to 2×10^{14} W/cm^2; even for the 60-μm spots and intensities in the 10^{15} W/cm^2 region lateral heat transport seems to be not dominant. In agreement with this consideration are the x-ray pinhole pictures of Fig. 9, which demonstrate that the radial hot plasma size equals the optical spot size. We note that the overdense layer thickness increases (approximately linearly) with the time during the short pulses (300 ps) considered here. With longer pulses

of a few ns duration it finally approaches a quasistationary value that is much larger. The short pulse used in this experiment is therefore favorable for negligible lateral heat flow.

We have also considered the divergence effect of the plasma flow to some extent by using one-dimensional spherical calculations. The radius (R_0) of curvature of the foil was set at twice the length of the spot diameter, as suggested in Ref. 58 on the basis of a comparison of real two-dimensional calculations with one-dimensional spherical calculations. High intensities with small spots are expected to show the largest effect. In fact, we find practically on influence on the simulation results at $\phi_{abs}=10^{14}$ W/cm^2 and $d_{spot}=400$ μm ($R_0=800$ μm), whereas at $\phi_{abs}\cong 10^{15}$ W/cm^2 and $d_{spot}=60$ μm ($R_0=120$ μm) an f value 0.02—0.03 is more appropriate than $f=0.01$ resulting from plane simulations to describe the experimental data.

Another point concerns the use of an ideal-gas equation instead of a real equation of state (EOS). For the medium-thickness case (as defined in Sec. IV A) the energy transferred to the foil is mainly kinetic energy caused by rocketlike foil acceleration, whereas the energy coupled into the shock wave is of minor importance. No influence due to EOS effects is therefore expected in this thickness range. Only for thick foils with dominating energy coupling into the foil (but $\eta \ll 1$) are corrections expected. But even in that case corrections are only important at lower pressures (generated at lower laser intensities) because then a real EOS predicts lower compression ratios ρ_1/ρ_0 with the consequence of a reduced η_s according to Eq. (9). Using published EOS data for plastic materials[59] one finds that this reduction may become important in the range $p\cong 0.1$—1 Mbar. As already mentioned in Sec. III D 2, EOS corrections are also important for the rear surface velocity v_R in the case of thick foils.

V. CONCLUSIONS

This paper describes a comprehensive series of experiments on foil acceleration in a wide intensity range at $\lambda=1.3$ μm. One major aspect was the study of the electron transport. In comparing the experimental data with the hydrodynamic code we found an indication of intensity-dependent flux inhibition. At lower intensities $\phi\leqq 10^{13}$ W/cm^2 the experiment is not in contradiction with $f\geqq 0.1$, whereas higher intensities $\phi\geqq 10^{14}$ W/cm^2 require $f\leqq 0.03$. The physics underlying this behavior is not yet clear, although many theoretical efforts have been made during the last few years to understand the electron energy transport in laser-produced plasmas.

The most natural attempt is an extension of the kinetic theory developed by Spitzer[54] to the case of steep temperature gradients.[60,61] These approximations yielded $f\cong 0.1$. As discussed in Sec. IV flux inhibition in the range $f=0.6$—0.1 has practically no effect on the numerical results (under the conditions of this experiment). It is therefore not clear if the reamining gap between $f=0.1$ found by kinetic theory and $f\leqq 0.03$ required for these experiments is caused by incorrect approximations or if completely different effects have to be considered.

Ion-acoustic turbulence has been proposed as a mechanism for flux inhibition.[62,63] Its importance, however, is unclear because computer simulations showed saturation of the ion-acoustic wave amplitudes at a rather low level insufficient to cause strong flux inhibition.[64]

Flux inhibition ($f=0.015$—0.03) was observed by us already at intensities $\cong 10^{14}$ W/cm^2. In this intensity range large spots (400 μm in diameter) were used, which resulted in a rather well-defined plane geometry for the short pulses (300 ps). In contrast, the highest intensities of this experiment ($\sim 5\times 10^{15}$ W/cm^2) are complicated by a small spot (60 μm in diameter), considerable hot-electron and fast-ion production, and lateral transport phenomena. The absorbed laser energy is essentially coupled into hot electrons with energies of about 20 keV and mean free path large compared with the plasma size. We could not confirm experimentally the naive expectation that the hot electrons are reflected at the vacuum plasma boundary and deposit their energy mainly in the dense target, whereas only a smaller energy fraction [of the order of $(Zm_e/m_i)^{1/2}$] is used for ion acceleration.[42,43] By different methods it was found that an amount small compared with the absorbed laser energy was deposited in the target: calorimetric measurements of the transfered energy exclude preheat levels above a few percent of the absorbed energy; the rear side ion blowoff decreased more strongly with foil thickness than expected for an uninhibited electron flux;[23] $K\alpha$ spectroscopy showed deposition of hot-electron energy in the dense target of only 3% of the absorbed energy.[25] It thus seems that by some mechanism the hot electrons are prevented from penetrating the dense target below the irradiated spot. Instead, a large energy fraction is found in fast ions (30% of the absorbed energy). Another fraction (10—20%) is transported laterally as found by $K\alpha$ photography (Fig. 21).

To describe this complicated situation theoretically, one has to consider electron groups of different energy, electrostatic fields necessary to drive return currents of cold electrons from the dense target into the corona for charge neutrality, and self-generated magnetic fields.[65—68] The complex models going in these directions have not been worked out for realistic experimental conditions and are therefore difficult to compare with experimental results. Experimentally, we obtained evidence of the presence of magnetic fields at high irradiation from the spatial structure observed in the $K\alpha$ emission from the region remote from the spot. As can be seen in Fig. 21 and more clearly in corresponding $K\alpha$ pictures obtained with more extended targets,[25] the remote $K\alpha$ emission becomes strongest at some distance (~ 1 mm) from the laser spot. This behavior, which was similarly observed in CO_2-laser experiments,[50,51] is attributed to annular magnetic fields surrounding the spot which may influence the lateral electron transport.[68] Magnetic field effects and the geometry of the plasma may be related to each other. It is not clear if magnetic fields are only important for the transport in strongly inhomogeneous plasmas obtained with small spots or if they are of more general importance also in cases of homogeneous illumination in large spots. In this context we note that transport experiments recently performed in spherical geometry[69] yielded evidence of

enhanced energy flux compared with planar experiments, which eventually may be caused by differences of the self-generated magnetic fields.

It seems that further progress towards an improved understanding of the microscopic processes underlying the reduced electronic energy transport calls for more specific investigations and also more powerful lasers for experiments closer to the idealized geometry of theoretical models. Although there are still questions left concerning the transport, we arrived at quite a good understanding of the hydrodynamic behavior. With a suitable value for the transport inhibition parameter, the observed hydrodynamic behavior is in agreement with the calculation, which is of great practical value because it allows us to describe the foil acceleration quantitatively. Besides, it has been demonstrated that pressures exceeding 10 Mbar and foil velocities of up to 10^8 cm/s by high-power laser irradiation can be generated. These conditions are of great interest for high-pressure physics and the acceleration of fast macroparticles. The detailed state of the accelerated foil material, its temperature, and density are of major importance for such applications and have to be studied in future experiments.

ACKNOWLEDGMENTS

The authors would like to thank F. Baldermann, H. Brändlein, C. Dorn, W. Fölsner, P. Sachsenmaier, and E. Wanka for skillful technical assistance. For the intensive work in making the iodine laser a useful tool in target experiments and for operating it, acknowledgment is due to the iodine laser team: Dr. G. Brederlow, H. Baumhacker, F. Denk, Dr. E. Fill, A. Herrle, G. Keller, H. Krause, Dr. R. Volk, and Dr. K. J. Witte. This work was supported in part by the Bundesministerium für Forschung und Technologie (Federal Republic of Germany) and by EURATOM.

APPENDIX A: RELATION BETWEEN TRANSFERED ENERGY AND ABLATED MASS

In this appendix we derive a formula for the energy transfer η which is modified compared with Eq. (1) by taking into account that the ablated plasma and the accelerated foil material are distributed over different velocities. It is reasonable to assume that, owing to expansion, original thermal energy is negligible when the accelerated foil arrives at the calorimeter. The mass of a fluid moment with velocities between v and $v+dv$ expanding into a solid angle $d\Omega$ can be written as

$$dM = F(v,\Omega)dv\,d\Omega\ ,$$

where $f(v,\Omega)$ takes into account the velocity and angular distribution of the mass elements. The total mass is

$$M = \int F(v,\Omega)dv\,d\Omega\ , \tag{A1}$$

the total momentum

$$I = \int F(v,\Omega)v\cos\vartheta\,dv\,d\Omega\ , \tag{A2}$$

and the total kinetic energy

$$E = \tfrac{1}{2}\int F(v,\Omega)v^2\,dv\,d\Omega\ . \tag{A3}$$

ϑ is the angle between the solid angle $d\Omega$ and the axis defined by the center of mass of the accelerated and the ablated material. The energy of the accelerated foil normalized to the total energy involved is given by

$$\eta = \frac{\int F_r v^2\,dv\,d\Omega}{\int F_r v^2\,dv\,d\Omega + \int F_f v^2\,dv\,d\Omega}\ , \tag{A4}$$

where F_r and F_f refer to the rear (accelerated foil) and front half spaces (ablated mass). The total energy in the denominator of Eq. (A4) is equivalent to the absorbed laser energy if radiation processes are not important, as is the case for the low-Z material considered here.

Taking into account the momentum balance

$$\int F_r v\cos\vartheta\,dv\,d\Omega = \int F_f v\cos\vartheta\,dv\,d\Omega$$

and using Eqs. (A2)–(A4), one finds Eq. (3) of Sec. III C:

$$\eta = \left[1+\gamma\left[\frac{m_F}{m_a}-1\right]\right]^{-1}\ .$$

The correction factor γ is given by

$$\gamma = \frac{\langle v_f^2\rangle\langle v_r\rangle^2}{\langle v_r^2\rangle\langle v_f\rangle^2}$$

with

$$\langle v\rangle = \frac{1}{M}\int Fv\cos\vartheta\,dv\,d\Omega\ ,$$

$$\langle v^2\rangle = \frac{1}{M}\int Fv^2\,dv\,d\Omega\ .$$

To calculate γ, the function $F(v,\Omega)$ has to be known. Analysis of the measured ion data and of two-dimensional high-speed photography shows that the effect of the angular distributions is of minor importance for γ. More important are the velocity distributions of the ablated hot plasma and the accelerated foil material, which are quite different. The velocity distribution of the ablated plasma has its maximum at $v=0$ and decreases as v increases. In contrast, the velocity distribution of the accelerated relatively cold foil material is peaked around the average velocity of the foil. Such behavior is indicated by the ion measurements using the results of Fig. 15 (one has to take recombination into account especially at low velocities) and is predicted by hydrodynamic calculations which give values of around 2 for γ. Mathematically one finds exactly $\gamma=2$ for a distribution at the front side of the type $F_f \propto e^{-v/v_0}$ and a δ-function-like distribution $F_r \propto \delta(v_0-v)$ at the rear side. Such an exponential distribution of the ablated plasma can be regarded as the result of an isothermal rarefaction wave which expands after the laser irradiation (compare, for example, Ref. 40).

APPENDIX B: REAR SIDE FOIL VELOCITY AND THE VELOCITY DETERMINED FROM CALORIMETER MEASUREMENTS

Here we discuss the relation between the calorimeter measurements and the rear side velocity obtained by high-speed photography. At the end of the laser pulse the energy transfered to the foil consists of thermal ($E_{\rm th}$) and

kinetic (E_{kin}) energy. The energy measured by the calorimeter can thus be written

$$E_{cal}=E_{kin}+E_{th} \tag{B1}$$

with $E_{kin}=(M/2)v_c^2$ (v_c is center-of-mass foil velocity). The thermal energy causes expansion of the foil with an expansion velocity observed in the frame of the moving foil given by (cf. Ref. 55)

$$v_{exp}=k_{exp}\left[\frac{E_{th}}{M}\right]^{1/2} . \tag{B2}$$

The number k_{exp} depends on the expansion mechanism and on the density observed by optical shadowgraphy. For example, for an ideal gas and an adiabatic expansion with an adiabatic coefficient equal to $\frac{5}{3}$ one finds for the front of the expanding gas $k_{exp}=\sqrt{10}$. The rear surface velocity v_R is given by

$$v_R=v_{exp}+v_c . \tag{B3}$$

For the ratio of v_R and the velocity $v_{cal}=(2E_{cal}/M)^{1/2}$ determined by calorimetry Eqs. (B1)—(B3) yield

$$\frac{v_R}{v_{cal}}=\frac{v_R}{v_c}\left[1+\frac{(v_R/v_c-1)^2}{k_{exp}^2/2}\right]^{-1/2} . \tag{B4}$$

Thus, if

$$\left[\frac{v_R}{v_c}-1\right]^2 \ll k_{exp}^2/2 ,$$

i.e., if v_R is sufficiently close to v_c, one has independently of the detailed expansion mechanism $v_{cal}\cong v_c$. The calorimeter value v_{cal} then directly measures the center-of-mass velocity. For larger values v_R/v_c the asymptotic value $v_R/v_{cal}\cong k_{exp}$ is approached, i.e., the calorimeter measures mainly thermal energy: $E_{cal}\cong E_{th}$.

---

*Present address: Ecole Polytechnique, F-91128 Palaiseau (Cédex), France.

†Present address: Department of Electrical Engineering, The University of Alberta, Edmonton, Alberta, Canada T6G 2G7.

‡Present address: European Southern Observatory, D-8046 Garching, Federal Republic of Germany.

§Present address: Psychiatrische Klinik der Universität München, Nussbaumstrasse 7, D-8000 München, Federal Republic of Germany.

**Present address: Brown Boveri Research Center, Abt. TCT-14, CH-5401 Baden, Switzerland.

††Present address: Shanghai Institute of Optics and Fine Mechanics, Academia Sinica, Shanghai, People's Republic of China.

[1]P. Mulser, R. Sigel, and S. Witkowski, Phys. Rep. **6C**, 189 (1973).

[2]J. Nuckolls, L. Wood, A. Thiessen, and G. Zimmermann, Nature (London) **239**, 139 (1972).

[3]H. Fechtig, E. Gruen, and J. Kissel, in *Cosmic Dust,* edited by J. A. M. McDonnel (Wiley, New York, 1978).

[4]S. L. Milora, J. Fusion Energy 1, 15 (1981).

[5]C. G. M. van Kessel and R. Sigel, Phys. Rev. Lett. **33**, 1020 (1974); C. G. M. van Kessel, Z. Naturforsch. **30a**, 1581 (1975).

[6]L. R. Veeser and J. C. Solem, Phys. Rev. Lett. **40**, 1391 (1978).

[7]R. J. Trainor, J. W. Shaner, J. M. Auerbach, and N. C. Holmes, Phys. Rev. Lett. **42**, 1154 (1979).

[8]S. I. Anisimov, A. M. Prokhorov, and V. E. Fortov, Sov. Phys.—Usp. **142**, 395 (1984).

[9]See, for example, *Laser-Plasma Interactions,* edited by R. A. Cairns and J. J. Sanderson (SUSSP, Edinburgh, 1980); *Laser-Plasma Interactions 2,* edited by R. A. Cairns (SUSSP, Edinburgh, 1983).

[10]B. H. Ripin, R. Decoste, S. P. Obenschain, S. E. Bodner, E. A. McLean, F. C. Young, R. R. Whitlock, C. M. Armstrong, J. Grun, J. A. Stamper, S. H. Gold, D. J. Nagel, R. H. Lehmberg, and J. M. McMahon, Phys. Fluids **23**, 1012 (1980).

[11]J. Grun, R. Decoste, B. H. Ripin, and J. Gardner, Appl. Phys. Lett. **39**, 545 (1981); J. Grun, S. P. Obenschain, B. H. Ripin, R. R. Whitlock, E. A. McLean, J. Gardner, M. J. Herbst, and J. A. Stamper, Phys. Fluids **26**, 588 (1983).

[12]S. P. Obenschain, R. R. Whitlock, E. A. McLean, B. H. Ripin, R. H. Price, D. W. Phillion, E. M. Campbell, M. D. Rosen, and J. M. Auerbach, Phys. Rev. Lett. **50**, 44 (1983).

[13]A. Raven, H. Azechi, T. Yamanaka, and C. Yamanaka, Phys. Rev. Lett. **47**, 1049 (1981).

[14]B. Arad, S. Eliezer, S. Jackel, A. Krumbein, H. M. Loebenstein, D. Salzmann, A. Zigler, H. Zmora, and S. Zweigenbaum, Phys. Rev. Lett. **44**, 326 (1980).

[15]B. Meyer, G. Morin, and G. Thiell, J. Appl. Phys. **53**, 2947 (1982).

[16]M. H. Key, W. T. Toner, T. J. Goldsack, J. D. Kilkenny, S. A. Veats, P. F. Cunningham, and C. L. S. Lewis, Phys. Fluids **26**, 2011 (1983).

[17]F. Amiranoff, R. Fabbro, E. Fabre, C. Garban, J. Virmont, and M. Weinfeld, Phys. Rev. Lett. **43**, 522 (1979).

[18]B. Yaakobi, T. Boehly, P. Bourke, Y. Conturie, R. S. Craxton, J. DeLettrez, J. M. Forsyth, R. D. Frankel, L. M. Goldman, R. L. McCrory, M. C. Richardson, W. Seka, D. Shvarts, and J. M. Soures, Opt. Commun. **39**, 175 (1981).

[19]H. D. Shay, R. A. Haas, W. L. Kruer, M. J. Boyle, D. W. Phillion, V. C. Rupert, H. N. Kornblum, F. Rainer, V. W. Slivinsky, L. N. Koppel, L. Richards, and K. G. Tirsell, Phys. Fluids **21**, 1634 (1978); W. C. Mead, E. M. Campbell, K. G. Estabrook, R. E. Turner, W. L. Kruer, P. H. Y. Lee, B. Pruett, V. C. Rupert, K. G. Tirsell, G. L. Stradling, F. Ze, C. E. Max, M. D. Rosen, and B. F. Lasinski, *ibid.* **26**, 2316 (1983).

[20]R. C. Malone, R. C. McCrory, and R. L. Morse, Phys. Rev. Lett. **34**, 721 (1975).

[21]Yung-lu Teng, R. Fedosejevs, R. Sigel, K. Eidmann, R. Petsch, and G. Spindler, Projektgruppe für Laserforschung (D-8046 Garching, Federal Republic of Germany), Report No. PLF 41 (October 1980) (unpublished).

[22]R. Fedosejevs, Yung-lu Teng, R. Sigel, K. Eidmann, and R. Petsch, J. Appl. Phys. **52**, 4186 (1981).

[23]G. D. Tsakiris, K. Eidmann, R. Petsch, and R. Sigel, Phys. Rev. Lett. **46**, 1202 (1981).

[24]K. Eidmann, A. G. M. Maaswinkel, R. Sigel, and S. Witkowski, Appl. Phys. B **28**, 295 (1982); S. Witkowski, F. Amiranoff, K. Eidmann, R. Fedosejevs, A. G. M. Maaswinkel, R. Sigel, and Yung-lu Teng, in *Proceedings of the Ninth*

Conference on Plasma Physics and Controlled Nuclear Fusion Research, Baltimore, 1982 (IAEA, Vienna, 1983), Vol. I, p. 155; F. Amiranoff, K. Eidmann, R. Fedosejevs, T. Kishimoto, A. G. M. Maaswinkel, R. Sigel, Yung-lu Teng, and S. Witkowski, Max-Planck-Institut für Quantenoptik (D-8046 Garching, Federal Republic of Germany), Report No. MPQ-59 (April 1982) (unpublished); in *Proceedings of the Japan-U.S. Seminar on Theory and Application of Multiply-Ionized Plasmas Produced by Laser and Particle Beams,* edited by C. Yamanaka (Institute of Laser Engineering, Osaka University, Osaka, 1982).

[25]F. Amiranoff, K. Eidmann, R. Sigel, R. Fedosejevs, A. G. M. Maaswinkel, Yung-lu Teng, J. D. Kilkenny, J. D. Hares, D. K. Bradley, B. J. McGowan, and T. J. Goldsack, J. Phys. D **15**, 2463 (1982).

[26]G. Brederlow, R. Brodmann, K. Eidmann, H. Krause, M. Nippus, R. Petsch, R. Volk, S. Witkowski, and K. J. Witte, Projektgruppe für Laserforschung (D-8046 Garching, Federal Republic of Germany), Report No. PLF-5 (July 1979) (unpublished); G. Brederlow, E. Fill, and K. J. Witte, *The High-Power Iodine Laser* (Springer, Berlin, 1983).

[27]K. Eidmann, G. Brederlow, R. Brodmann, R. Sigel, R. Volk, S. Witkowski, and K. J. Witte, Projektgruppe für Laserforschung (D-8046 Garching, Federal Republic of Germany), Report PLF 4 (January 1978) (unpublished).

[28]R. Petsch, Projektgruppe für Laserforschung (D-8046 Garching, Federal Republic of Germany), Report PLF 27 (February 1980) (unpublished).

[29]R. P. Godwin, P. Sachsenmaier, and R. Sigel, Phys. Rev. Lett. **39**, 1198 (1977).

[30]K. Eidmann, G. Brederlow, R. Brodmann, R. Petsch, R. Sigel, G. Tsakiris, R. Volk, and S. Witkowski, J. Phys. D **12**, L145 (1979).

[31]J. W. Murdoch, J. D. Kilkenny, D. R. Gray, and W. T. Toner, Phys. Fluids **24**, 2107 (1981).

[32]Vm. J. Veigele, E. Briggs, L. Bates, E. M. Henry, and R. Bracewell, Kaman Sciences Cooperation (Colorado) Report No. KN-71-431(R), July 1971 (unpublished).

[33]A. J. Meyrott, P. C. Fisher, and D. T. Roethig, Rev. Sci. Instrum. **35**, 669 (1964); K. J. Roulston and S. J. H. Nagvi, Nucleonics **15**, 86 (1957).

[34]K. Eidmann, M. H. Key, and R. Sigel, J. Appl. Phys. **47**, 2402 (1976); K. A. Brueckner, Phys. Rev. Lett. **36**, 677 (1976).

[35]G. H. McCall, J. Phys. D **15**, 823 (1982).

[36]R. R. Goforth and P. Hammerling, J. Appl. Phys. **47**, 3918 (1976).

[37]M. K. Matzen and J. S. Pearlman, Phys. Fluids **22**, 449 (1979).

[38]J. S. Pearlman, Rev. Sci. Instrum. **48**, 1064 (1977).

[39]R. Decoste and B. H. Ripin, Phys. Rev. Lett. **40**, 34 (1978).

[40]L. M. Wickens, J. E. Allen, and P. T. Rumsby, Phys. Rev. Lett. **41**, 243 (1978).

[41]N. A. Ebrahim, C. Joshi, D. M. Villeneuve, N. H. Burnett, and M. C. Richardson, Phys. Rev. Lett. **43**, 1995 (1979).

[42]W. L. Kruer, Comments Plasma Phys. **5**, 69 (1979).

[43]R. Sigel, in *Laser-Plasma Interactions 2,* see Ref. 9.

[44]S. R. Gunn and V. C. Rupert, Rev. Sci. Instrum. **48**, 1375 (1977).

[45]W. Eckstein and H. Verbeek, Max-Planck-Institut für Plasmaphysik (D-8046 Garching, Federal Republic of Germany), Report No. IPP 9/32 (August 1979) (unpublished).

[46]K. B. Mitchell and R. P. Godwin, J. Appl. Phys. **49**, 3851 (1978).

[47]T. Kishimoto, Max-Planck-Institut für Quantenoptik (D-8046 Garching, Federal Republic of Germany), Report No. MPQ 76 (July 1983) (unpublished).

[48]Y. L. Teng, R. Fedosejevs, and R. Sigel, Max-Planck-Institut für Quantenoptik (D-8046 Garching, Federal Republic of Germany), Report No. MPQ 43 (March 1981) (unpublished).

[49]F. C. Jahoda and G. A. Sawyer, in *Methods of Experimental Physics,* edited by L. Marton (Academic, New York, 1971), Vol. 9B, pp. 1—48.

[50]This feature was recently confirmed by shadowgrams of single- and double-foil targets obtained with an improved technique [A. G. M. Maaswinkel, K. Eidmann, R. Sigel, and S. Witkowski (unpublished)].

[51]P. A. Jaanimagi, N. A. Ebrahim, N. H. Burnett, and C. Joshi, Appl. Phys. Lett. **38**, 734 (1981); M. A. Yates, D. B. van Hulsteyn, H. Rutkowski, G. Kyrala, and J. U. Brackbill, Phys. Rev. Lett. **49**, 1702 (1982).

[52]R. Schmalz, private communication based on hydrodynamic calculations including a real equation of state.

[53]R. F. Schmalz, P. Mulser, and G. Spindler, Max-Planck-Institut für Quantenoptik (D-8046 Garching, Federal Republic of Germany), Report No. MPQ 75 (July 1983) (unpublished).

[54]L. Spitzer, *Physics of Fully Ionized Gases* (Interscience, New York, 1956).

[55]Ya. B. Zel'dovich and Yu. P. Raizer, *Physics of Shock Waves and High-Temperature Hydrodynamic Phenomena,* edited by W. D. Hayes and R. F. Probstein, English translation (Academic, New York, 1967).

[56]W. M. Manheimer, D. G. Colombant, and J. H. Gardner, Phys. Fluids **25**, 1644 (1982).

[57]P. D. Roberts and P. C. Thompson, in *Proceedings of the 15th European Conference on Laser Interaction with Matter,* Schliersee, Federal Republic of Germany, January 1982 (unpublished).

[58]W. C. Mead, E. M. Campbell, K. G. Estabrook, R. E. Turner, W. L. Kruer, P. H. Y. Lee, B. Pruett, V. C. Rupert, K. G. Tirsell, G. L. Stradling, F. Ze, C. E. Max, and M. D. Rosen, Phys. Rev. Lett. **18**, 1289 (1981).

[59]B. J. Bennet, J. D. Johnson, G. J. Kerley, and G. T. Rood, Los Alamos Scientific Laboratory (University of California, Los Alamos, New Mexico, U.S.A.), Report No. LA-7130 February 1978 (unpublished).

[60]A. R. Bell, R. G. Evans, and D. J. Nicholas, Phys. Rev. Lett. **46**, 243 (1981).

[61]D. Shvarts, J. Delettrez, R. L. McCrory, and C. P. Verdon, Phys. Rev. Lett. **47**, 247 (1981).

[62]D. W. Forslund, J. Geophys. Res. Space Phys. **75**, 17 (1979).

[63]W. M. Manheimer, Phys. Fluids **20**, 265 (1977).

[64]W. C. Mead, in Proceedings of the Centre Européen de la Calcule Atomic et Moleculaire Workshop on Fast Electron Transport, Orsay, France, August 14—31, 1979 (unpublished).

[65]D. Shvarts, C. Yablon, I. B. Bernstein, J. Virmont, and P. Mora, Nucl. Fusion **19**, 1457 (1979).

[66]R. J. Mason, Phys. Rev. Lett. **42**, 239 (1979).

[67]R. J. Mason, Phys. Rev. Lett. **43**, 1795 (1979).

[68]D. W. Forslund and J. U. Brackbill, Phys. Rev. Lett. **48**, 1614 (1982).

[69]T. J. Goldsack, J. D. Kilkenny, B. J. MacGowan, P. F. Cunningham, C. S. Lewis, M. H. Key, and P. T. Rumsby, Phys. Fluids **25**, 1634 (1982); J. A. Tarvin, W. B. Fechner, J. T. Larsen, P. D. Rocket, and D. C. Slater, KMS Fusion Report No. KMSF U-1303, 1983 (unpublished).

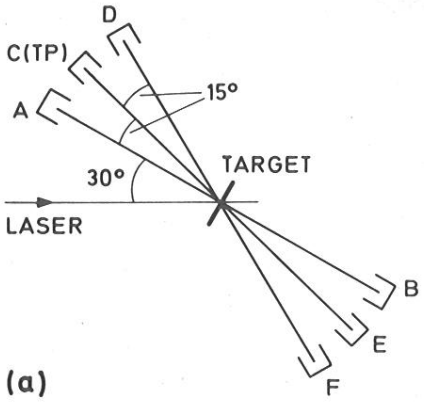

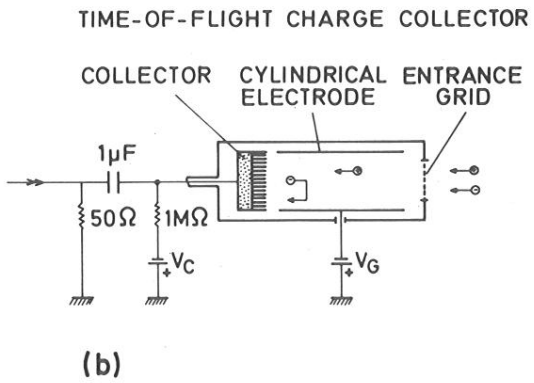

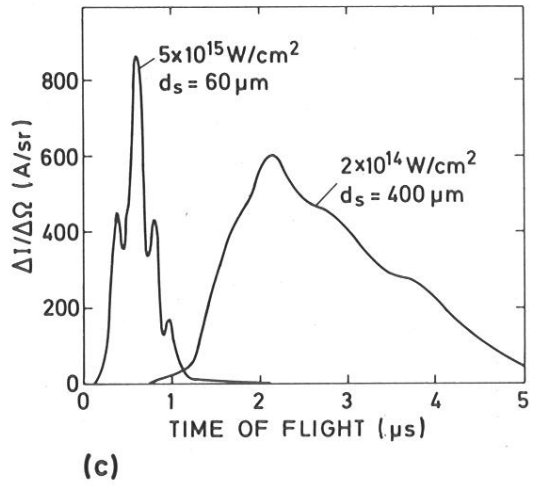

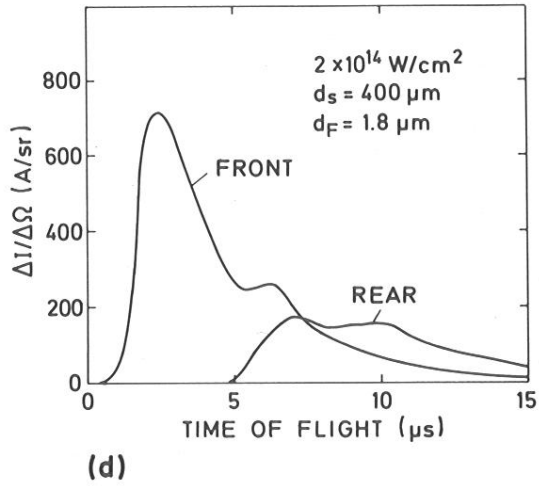

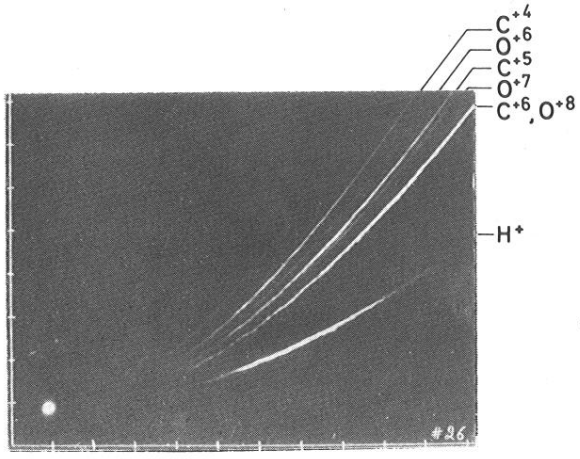

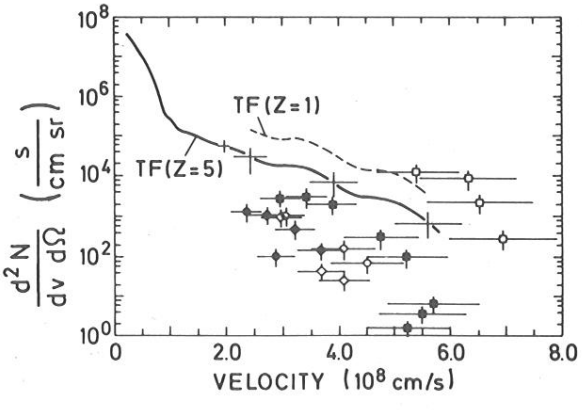

FIG. 14. Ion diagnostics. (a) Arrangement of detectors around the target. (b) Setup of a TOF detector. (c) TOF signal at different intensities (front collector A). (d) TOF signal at front and rear side (collectors A and B), $d_F = 1.8$ μm, $\phi_{inc} = 2\times10^{14}$ W/cm^2. (e) Thomson parabolas recorded on cellulose nitrate film (4×10^{15} W/cm^2). (f) Ion velocity distribution from TOF [curves TF($Z=1$) and TF ($Z=5$)] and TP (□, H^{1+}; ■, O^{8+}, N^{7+}, C^{6+}; ○, O^{7+}; ●, O^{6+}; ◇, N^{6+}; ◇, N^{5+}) (4×10^{15} W/cm^2).

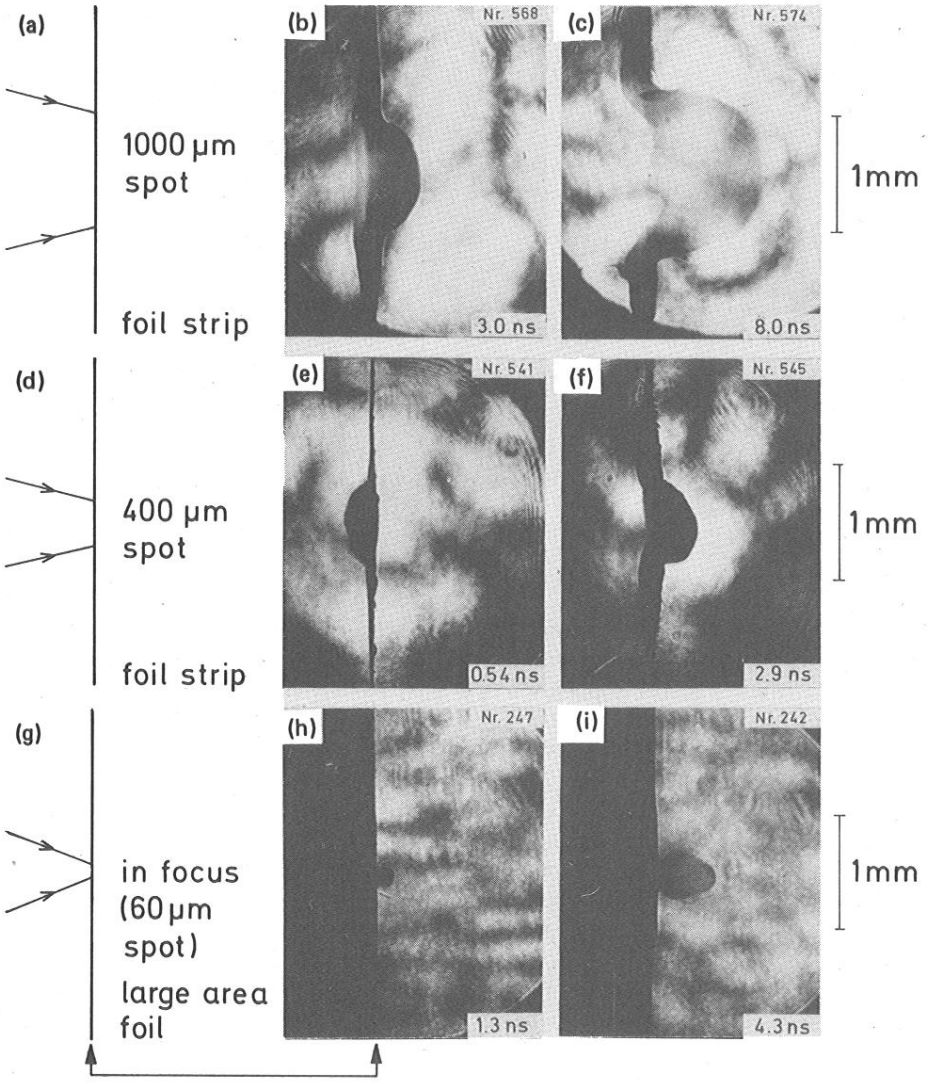

FIG. 20. Shadowgrams at different times and different spot sizes. $E_{inc} \cong 70-100$ J. Times are with respect to the maximum of the iodine laser pulse. Target: (a)—(c), 1000-μm-wide Makrofol strip, 1.8 μm thick; (d)—(f), 400—500-μm-wide Makrofol strip, 1.8 μm thick; (g)—(i), extended Makrofol foil, 20 μm thick (in this case the foil was slightly curved in order to get a sharp picture of the rear foil surface; the front side is shadowed by the foil itself and therefore not visible).

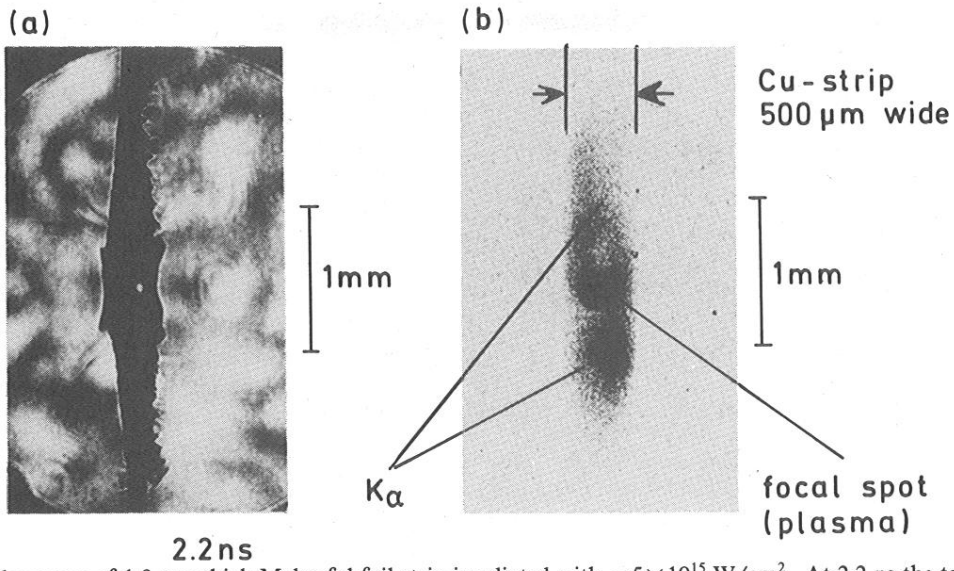

FIG. 21. (a) Shadowgram of 1.8-μm-thick Makrofol foil strip irradiated with $\cong 5\times 10^{15}$ W/cm^2. At 2.2 ns the target is seen to explode over the whole field of view. (b) $K\alpha$ pinhole picture of a 500-μm-wide Cu strip. Pinhole diameter 200 μm with 11-μm-thick Cu filter. $\phi_{\text{inc}} \cong 5\times 10^{15}$ W/cm^2.

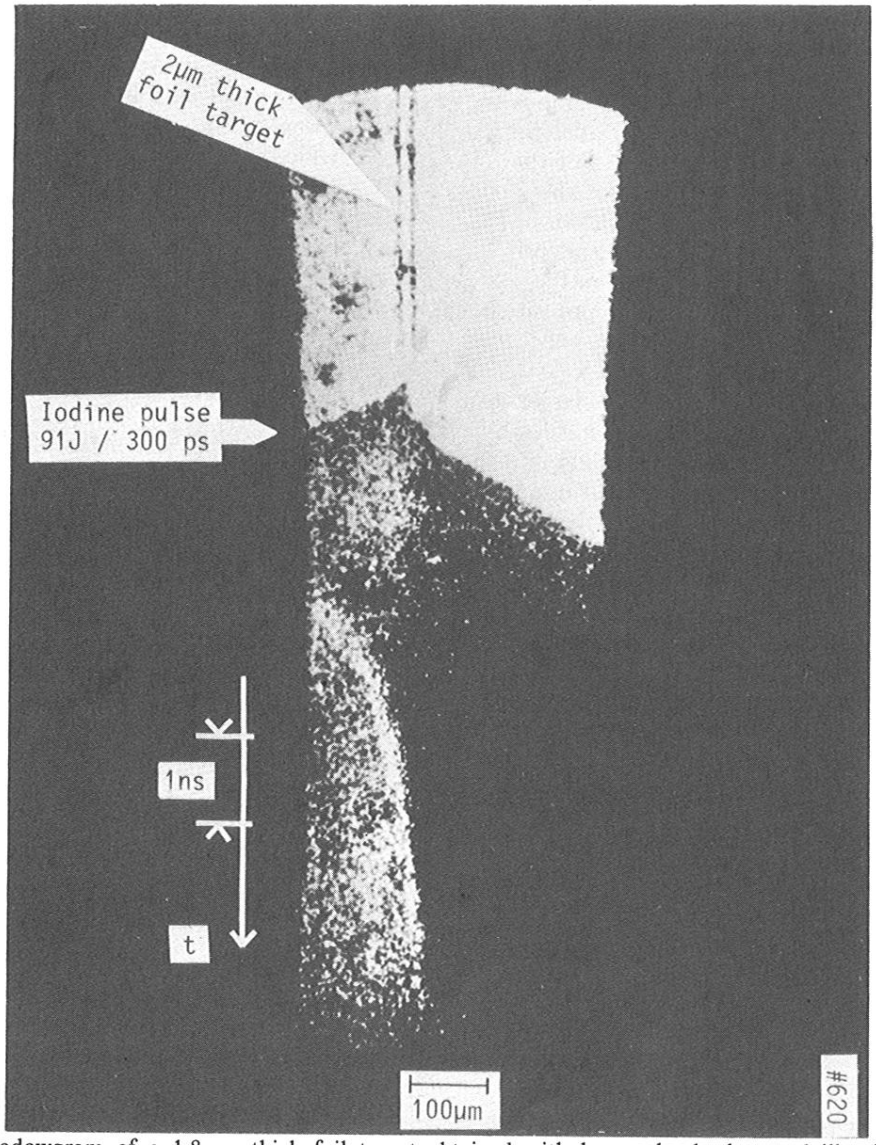

FIG. 22. Streak shadowgram of a 1.8-μm-thick foil target obtained with long-pulse background illumination. $\phi_{inc}=2\times10^{14}$ W/cm^2.

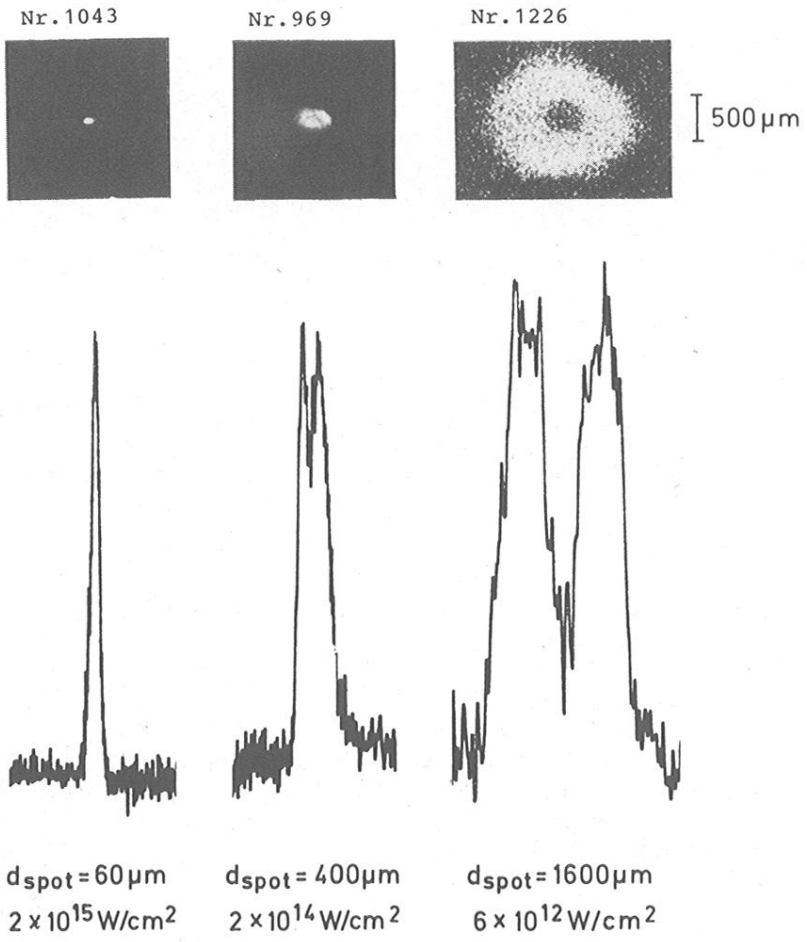

FIG. 9. X-ray pinhole pictures at different spot sizes (observed at 45° to the laser axis from the front side, 12-μm pinhole, 25-μm Be as filter).